

Quantifying frost weathering induced ~~rock~~ damage in ~~high~~ alpine ~~rockwalls~~rocks

Till Mayer^{1,2}, Maxim Deprez³, Laurenz Schröer³, Veerle Cnudde^{3,4}, Daniel Draebing^{5,1}

¹ Chair of Geomorphology, University of Bayreuth, 95447 Bayreuth, Germany.

5 ² Chair of Landslide Research, Technical University of Munich, 80333 Munich, Germany

³ Department of Geology, University Gent, 9000 Gent, Belgium.

⁴ Department of Earth Sciences, Utrecht University, 3584 CB Utrecht, Netherlands.

⁵ Department of Physical Geography, Utrecht University, 3584 CB Utrecht, Netherlands.

10 *Correspondence to:* Till Mayer (till.mayer@uni-bayreuth.de)

Abstract. Frost weathering is a key mechanism of rock failure in periglacial environments and landscape evolution. At high alpine rockwalls, freezing regimes are a combination of diurnal and sustained seasonal freeze-thaw regimes and both influence frost cracking processes. Recent studies have tested the effectiveness of freeze-thaw cycles by measuring weathering proxies for frost damage in low-strength and grain-supported pore space rocks, but detecting frost damage in low-porosity and crack-dominated alpine rocks is challenging due to small changes in these proxies that are close to the detection limit. Consequently, the assessment of frost weathering efficacy in alpine rocks may be flawed. In order to fully determine the effectiveness of both freezing regimes, freeze-thaw cycles and sustained freezing were simulated on low-porosity high-strength Dachstein limestone ~~under temperature and moisture conditions that reflect those found in high alpine rockwalls with varying saturation.~~ Frost-induced rock damage was uniquely quantified by combining X-ray computed micro-tomography (μ CT), acoustic emission (AE) monitoring and frost cracking modelling. To differentiate between potential mechanisms of rock damage, thermal- and ice-induced stresses were simulated and compared with AE activity. ~~μ CT combined with AE data revealed frost damage on low porosity alpine rocks with crack growth along pre-existing cracks with magnitudes dependent on the initial crack density. It was observed that diurnal freeze-thaw cycles have a higher frost cracking efficacy on alpine rocks compared to a seasonal sustained freezing regime. On north facing high alpine rockfaces, the number of freeze-thaw cycles and the duration of sustained freezing conditions vary with elevation and seasonal climate. The experimental results establish a link between frost damage and elevation dependent rockwall erosion rates, which has implications for hazard prediction in mountainous areas under a changing climate. Our results underscore the significant impact of initial crack density on frost damage, with μ CT scans revealing damage primarily through crack expansion. Discrepancies between AE signals and visible damage indicate the complexity of damage mechanisms. The study highlights frost cracking as the main driver of rock damage during freezing periods. Notably, damage is more severe during repeated freeze-thaw cycles compared to extended periods of freezing, a finding that diverges from field studies. This discrepancy could stem from limited water mobility due to low porosity or the short duration of our experimental setup.~~

15
20
25
30

35 **Keywords.** Frost weathering, ~~micro-CT~~μCT, periglacial processes, frost cracking modelling, rock damage

1 Introduction

Frost weathering is a key mechanism for rock breakdown in periglacial environments (Matsuoka and Murton, 2008) and is therefore considered to be the main driver for alpine landscape evolution (Egholm et al., 2015; Hales and Roering, 2009). The
40 breakdown of rock due to freezing is called frost cracking and can prepare and trigger rockfall (Matsuoka, 2019). Cracking can occur when stresses exceed thresholds (critical cracking) or by repetition of low magnitude stresses that progressively weaken the rock (subcritical cracking; Eppes and Keanini, 2017). Frost cracking was associated with two different processes: volumetric expansion and ice segregation (Matsuoka and Murton, 2008).

~~When water freezes to ice~~ volumetric expansion of 9% occurs ~~when water freezes to ice~~ and can theoretically build up stresses
45 of up to 207 MPa (Matsuoka and Murton, 2008), which would exceed the tensile stress of most existing rock (Perras and Diederichs, 2014). Conditions that favour volumetric expansion are a high degree of water saturation of 91 % (Walder and Hallet, 1986), a rapid freezing associated with diurnal freeze-thaw cycles (Matsuoka, 2001; Matsuoka and Murton, 2008) and a freezing from all sides (Matsuoka and Murton, 2008). However, ~~rock conditions facilitating volumetric expansion in real rockwalls are rare as~~ moisture conditions exceeding 91 % are rarely given ~~in alpine rockwalls during phases of rapid freezing~~
50 ~~(Sass, 2005a) during time periods of diurnal freezing, e.g. in autumn or spring or during sustained freezing in winter (Fig. 2b).~~ ~~In addition, topography influences the temperature regime of rockwalls and therefore their freezing behaviour (Noetzi et al., 2007), making freezing from all sides unlikely. Therefore, the conditions for volumetric expansion are unlikely in alpine rock faces, and any stresses inducing rock failure may result from ice segregation. Laboratory studies have observed a decrease in elastic and mechanical properties after frequent freeze thaw cycles, which has been interpreted as rock fatigue or subcritical cracking due to volumetric expansion. However, these studies do not provide insight into the timing of cracking and cannot exclude the influence of alternative cracking processes such as thermal stress or ice segregation by water migration towards ice crystals.~~

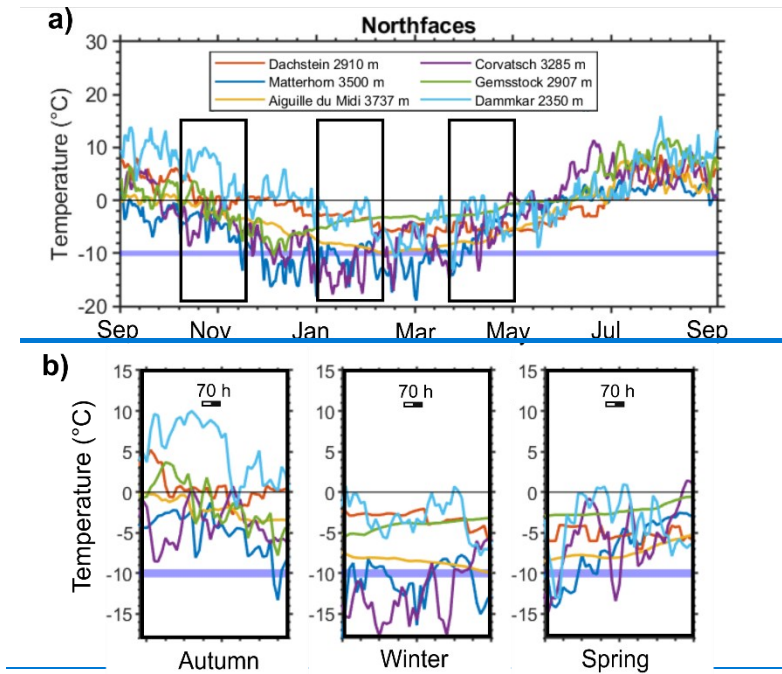
~~Under~~During freezing ~~conditions, an processes,~~ ice ~~crystal forms in crystals develop within~~ cracks and pores. ~~Due to repulsive forces of rock. A repulsion mechanism ensures that~~ a thin water film (<9 nm) ~~film of water remains persists~~ between the ice crystal and the walls of the pore or crack ~~wall~~ (Gilpin, 1979; Webber et al., 2007; Sibley et al., 2021), ~~allowing water flow driven by a thermodynamic potential gradient from either facilitating the movement of unfrozen rock or unfrozen water present within the frozen rock matrix towards the ice crystal driven by a thermodynamic potential gradient (Derjaguin and Churaev, 1986; Kjelstrup et al., 2021; Everett, 1961; Gerber et al., 2022). This process is called~~ Due to ice segregation ~~and the pressure generated by the growth of,~~ ice expands within pores and cracks ~~is called crystallisation and generates crystallization~~ pressure
65

(Scherer, 1999) and is the main driver of ice segregation induced rock failure, known as frost cracking. Ice segregation can occur in low saturated rock and is associated with seasonal freezing. demonstrated that the presence of permafrost enhances ice segregation by refreezing rock moisture at the permafrost table caused by active layer thawing. The temperature range in which ice segregation is most efficient is that can damage rocks. Ice segregation is most efficient in a temperature range called the 'frost cracking window' (Anderson, 1998) and which depends on rock strength (Walder and Hallet, 1985; Mayer et al., 2023). Common temperature ranges vary from -6 to -3 °C for low-strength Berea sandstone (Hallet et al., 1991), but can drop to -15 to -5°C for high-strength rocks (Walder and Hallet, 1985; Mayer et al., 2023). Therefore, Ice segregation can occur in low-saturated rock (Mayer et al., 2023) and is theoretically favoured more conducive in environments characterized by low slow freezing rates and sustained freezing continuous low temperatures occurring during typical of seasonal freezing (Matsuoka and Murton, 2008; Walder and Hallet, 1986).

Frost cracking serves as an indicator for assessing frost damage or the increase in porosity in rocks and rockwalls, yet its gradual and subcritical nature makes direct measurements challenging. Consequently, laboratory studies have adopted indicators such as AE signals (Hallet et al., 1991; Mayer et al., 2023; Maji and Murton, 2021; Duca et al., 2014), frost heave or crack expansion (Murton et al., 2006; Draebing and Krautblatter, 2019), alterations in mechanical properties like p-wave velocity, Youngs' Modulus, uniaxial strength or porosity (Whalley et al., 2004; Matsuoka, 1990; Jia et al., 2015; Eslami et al., 2018; Prick, 1997), and frost cracking simulations (Mayer et al., 2023; Murton et al., 2006) to estimate its impact. At the scale of rockwalls, proxies such as AE signals (Girard et al., 2013; Amitrano et al., 2012), fracture density (Hales and Roering, 2009; Draebing and Mayer, 2021; Messenzehl et al., 2018), fracture opening (Draebing, 2021; Draebing et al., 2017b; Draebing et al., 2017a), rockwall erosion rates (Draebing et al., 2022; Matsuoka, 2008), as well as frost cracking simulations (e.g. Draebing et al., 2022; Sanders et al., 2012) In alpine catchments, frost cracking activity is difficult to assess. used acoustic emission (AE) to monitor frost cracking, but other thermal stress induced cracking processes cannot be excluded as alternative sources of AE signals. Most commonly, frost cracking is modelled using simulations with a fixed frost cracking window between -8 and -3 °C or a rock strength dependent frost cracking window and applying an elevation dependent air temperature as a proxy for rockwall temperatures. However, topographic effects in mountain rockwalls affect insolation by exposition and snow cover duration, therefore, rock surface temperatures differ from air temperatures in the magnitude of temperatures and frequency of freeze thaw cycles. To account for topographic effects, previous studies have used recorded rock temperatures to drive frost cracking models and validated models with fracture spacing measurements or rockwall erosion rates derived by terrestrial laser scanning. With increasing elevation and hence colder prevailing temperatures, frost cracking models indicate an increase in frost cracking activity up to an elevation range, where temperatures are sufficiently cold to limit water transport towards ice lenses. These elevations are characterised by long periods of sustained freezing (e.g. Matterhorn, Aiguille di Midi in Fig. 1a-b and Fig. 2a), in contrast to lower elevation rockwalls where frequent freeze thaw cycles are common (e.g. Dammkar in Fig. 1e and Fig. 2a).



Figure : Selected alpine rockwalls a) Aiguille du Midi (Mont Blanc Massif, French Alps), b) Matterhorn (Valais, Swiss Alps) c) Corvatsch (Engadin, Swiss Alps), d) Gemsstock (Uri, Swiss Alps), e) Dachstein (Northern-Calcareous Alps, Austria) and f) Dammkar (Northern-Calcareous Alps, Germany) used for the analysis of freezing regimes in Fig. 2.



105 **Figure 2: a b) Diurnal freeze thaw cycles and sustained freezing based on measured rock surface temperatures in 10 cm depth at**
north-facing rockwalls for Matterhorn 2017/18 , Aiguille du Midi 2014/15 , Corvatsch 2020/21 , Gemsstock 2017/18 , Dachstein and
Dammkar 2020/21 (unpublished own data). The lilac bold line indicates -10°C , the applied lower rock temperature boundary of our
experimental set up.

110 ~~quantified ice induced stresses by volumetric expansion and ice segregation in rock samples with a mode I cracks, and describe~~
~~the mechanisms of ice induced fracture opening in the field . The stresses generated by ice segregation were below the rock~~
~~strength threshold and therefore in the subcritical cracking range . Currently, stresses can be calculated using mechanical~~
~~models, or rock damage can be estimated using proxies such as decreases of p wave velocity or Young's modulus or small~~
~~increases in porosity . However, in low porosity rocks have been utilized to infer frost cracking activity. However, all these~~
115 ~~techniques provide proxies for frost cracking and as low-porosity alpine rocks are characterized by micro-cracks, changes in~~
~~frost cracking proxies are very small and often within the uncertainty of the techniques used, and therefore do not provide~~
~~reliable results. In contrast, X-ray computed micro-tomography (μCT) enables the quantification of material damage (Cnudde~~
~~and Boone, 2013; Withers et al., 2021) and was previously applied to track frost cracking damage in high-porosity rocks (De~~
~~Kock et al., 2015; Deprez et al., 2020a; Maji and Murton, 2020; Dewanckele et al., 2013) or assess post-experimental frost~~
120 ~~damage along artificial cracks in low- porosity rocks (Wang et al., 2020a; 2020b) exposed to frequent freeze-thaw cycles.~~

To our knowledge, no study has directly quantified ~~rock damage and hence~~ the effectiveness of ~~freeze thaw cycles in inducing~~
~~frost cracking. Furthermore, laboratory different~~ freeze-thaw ~~tests have never~~ cycles or demonstrated whether frost cracking
creates new cracks or propagates existing cracks in high-strength, ~~intact, low porosity rock. low porosity rocks. In this study,~~
~~we exposed low-porosity, high-strength Dachstein limestone to frequent diurnal and seasonal sustained freeze-thaw cycles~~

125 during laboratory freezing experiments. We monitor acoustic emission events during the experiments and modelled thermal and ice-induced stresses and applied μ CT to pre- and post-stressed rocks to quantify and track crack propagation and to assess frost cracking efficacy of different freeze-thaw cycles.

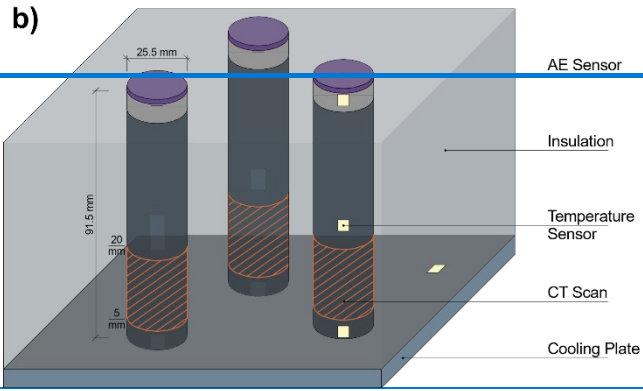
In this study, we tested the efficacy of frequent diurnal and sustained seasonal freeze-thaw cycles reflecting temperature conditions in high alpine rockwalls (Fig. 2a b) on low porosity, high strength Dachstein limestone. For this purpose, we
130 conducted laboratory freezing experiments while monitoring acoustic emission events and modelling thermal and ice induced stresses. To assess frost cracking efficacy, we applied X-ray computed micro-tomography (μ CT) to identify and quantify crack propagation.

2 Material and Methods

135 2.1 Rock samples and mechanical properties

We collected three large ~~rock~~ boulders ~~from a scree slope adjacent to a north facing rockwall located at 2650 m of Dachstein limestone~~ in the Dachstein mountain range, Austria. Dachstein limestone (upper Triassic) is a massive rock with minor occurrence of fractures which is widespread in the Northern-Calcareous Alps (Pfiffner, 2010). ~~From boulder one,~~ we drilled three cylindrical samples with ~~a size of~~ 10 cm (in length) x 5 cm (in diameter) and measured rock density ρ_r and open porosity
140 n_r by immersion weighing (DIN-EN 52102:2006-02; DIN-EN 1097-6:2022-5) ~~(DIN 52102 and DIN EN 1097-6)~~. The determined rock density was 2690 kg m⁻³ and rock porosity 0.1% (Table 1). To quantify shear modulus G , Poisson' ratio ν and Young's modulus E , dilatational wave velocity ~~(V_D)~~ measurements were performed using a Geotron ultrasonic generator USG40 and a Geotron preamplifier VV51 with 20 kHz sensors. Sensor to sample coupling was improved by applying 0.2 MPa pressure. Detection and analyses of the signals were proceeded with a PICO oscilloscope and the software Geotron Lighthouse
145 DW. Determined values of shear modulus were 24.02 \pm 0.05 GPa, Poisson' ratio 0.327 \pm 0.003 and Young's modulus 63.74 \pm 0.04 GPa (Table 1). We drilled two cylindrical samples with a size of 5 x 2.5 cm from boulder one to measure tensile strength σ_t following Lepique (2008). The determined tensile strength was 7.9 \pm 0.7 MPa. Fracture toughness K_{IC} was tested in the Magnel-Vandepitte Laboratory at Ghent University using a three-point bending ~~(TPB)~~ test setup on boulder two (Carloni et al., 2019; Bazant and Planas, 1998). For Dachstein limestone the fracture toughness was 1.32 \pm 0.1 MPa m^{1/2}. ~~At~~ For the
150 freezing experiments were conducted on we drilled six 91.5 x 25.5 mm large cylindrical samples 91.5 mm long and 25.5 mm in diameter from boulder three (Fig. 3a) drilled 1b) to keep micro-fractures as homogenous as possible. We assume that mechanical properties from the three rock boulders are identical as they were collected from the same rock boulder/rockwall.

a) Freeze-Thaw cycles (FT-1) Sustained Freezing cycle (FT-2)



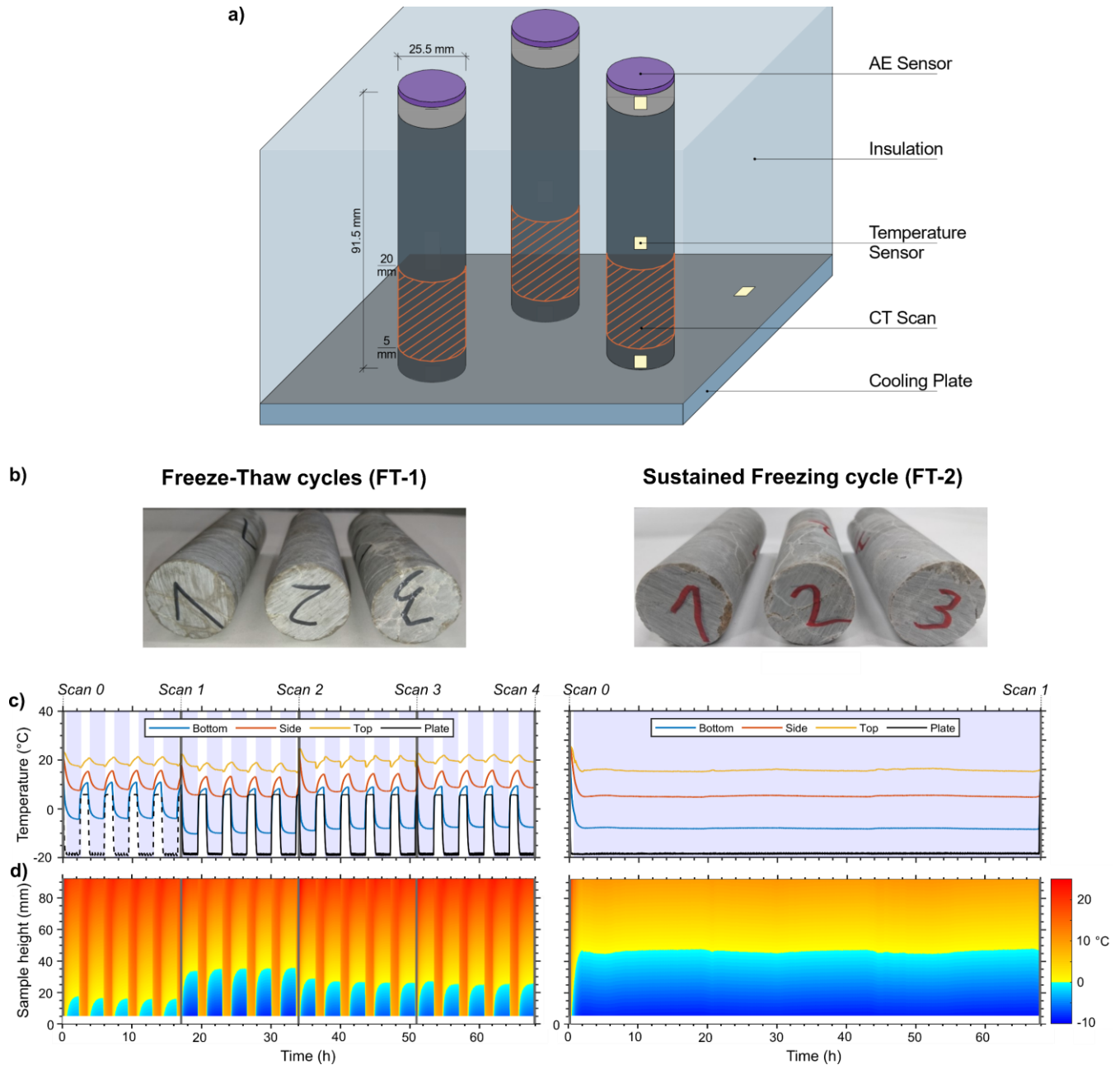


Figure 1: The design of the experiment was influenced by the methodologies of Hallet et al. (1991) and Mayer et al. (2023). a) 91.5 x 25.5 mm large cylindrical Dachstein limestone samples used for freeze-thaw experiments. b) focusing on distinguishing ice segregation as a distinct weathering process from other weathering mechanisms. a) Schematic representation of freezing laboratory setup. We established created a linear temperature gradient by cooling three rock samples, each with different degrees varying levels of saturation with, using a cooling plate positioned at the bottom, while exposing the top of these the samples was exposed to ambient room temperature conditions. b) 91.5 x 25.5 mm large cylindrical Dachstein limestone samples used for freeze-thaw experiments. c) temperature cycles were implemented for FT-1 and FT-2, along with the corresponding measurements of rock and cooling plate

165 temperatures. In FT-1, between scan 0 and 1, there was inadequate coupling of the temperature sensor, resulting in excessively high temperature readings. d) temperature isoplots of derived temperature distribution within the sample.

2.2 Freezing experiments setup

We tested six samples (Fig. 3a) in two different experiments in which three samples were exposed to multiple freeze-thaw cycles (FT 1) and three samples to a sustained freezing cycle (FT 2, see sites with temperatures below 0°C in Fig 2a).

170 Saturation of the samples was conducted by immersing the lower part of the rock samples into a distilled water bath. To prevent air inclusions, we raised slowly the water table until samples were completely immersed, and a constant mass was prevailing (we refer to as 100 % or fully saturated). Subsequently, samples were dried under atmospheric conditions and weighed until a saturation of 30 % or 70 % was reached. To prevent rock moisture loss due to evaporation, the samples were wrapped in clingfilm during the experiment. The samples were placed Three rock samples were placed at the same time into an insulating

175 holder on a cooling plate, which was driven by Peltier elements (TE technology, CP-121HT), a power supply unit (PS-24-13), and a temperature control system (TC-48-20 OEM, Fig. 3b1a). While the bottom part was exposed to freezing conditions from the cooling plate, the top part was left open to non-freezing ambient laboratory conditions (~ 20 °C). With this setup we simulated an open/closed system that provides a linear temperature gradient and a water body inside the rock samples reflecting natural rockwall conditions. Frost cracking efficacy was tested by applying two different experimental cooling cycles. For the first freeze-thaw experiment (FT 1), the cooling plate was oscillating between 20 °C (2 hours) and 5 °C (1 hour). In total, the FT 1 lasted for 68 h and cycled 20 times between freezing and thawing conditions. In the second experiment, a sustained freezing cycle (FT 2) was applied by setting the cooling plate to 20 °C for 68 h. The cooling plate temperature of 20 °C provided a rock surface temperature at the bottom of the sample of 10 °C, which reflected north facing rockwall conditions (Fig. 2a).

185 simplified natural rockwall conditions. During the freezing experiments, rock temperature was monitored every minute at the side close to the top, middle and close to the bottom of one rock sample with three SE060 high temperature type K thermocouples (accuracy ± 0.5 °C, Pico Technology, Fig. 1b) to avoid damaging the samples by drilling. The surface temperature of the sample has a slight offset compared to the internal temperature at the centre, with lower temperatures in the core of the sample. However, we assume this offset as minor due to the high thermal conductivity of limestone (2.4 Wm⁻¹K⁻¹ (Cermák and Rybach, 1982)3b). An additional thermocouple was placed onto the cooling plate to record cooling plate temperatures. To test the efficiency of freeze-thaw cycles, we exposed three rock samples at the same time to two different freeze-thaw cycles.

195 As saturation influences frost weathering, we used rock samples with an initial saturation of approximately 30, 70 and 100 % categorized as low, partially, and highly saturated, respectively. The samples were saturated by immersing the lower part into a distilled water bath. To prevent air inclusions, we raised slowly the water table until samples were completely immersed, and a constant mass was prevailing (we refer to as highly saturated). Subsequently, samples were dried under atmospheric conditions, weighed until low (30 %) or partially saturation (70 %) was reached. To minimize moisture loss through

evaporation, the samples were wrapped in clingfilm. As porosity of the samples is 0.1 %, the level of saturation is inaccurate and provide only a rough estimation. Furthermore, the saturation can change during the experiments due to moisture loss or distribution of rock moisture can alter within the rock samples. We chose the length of the rock samples of 91.5 mm to enable moisture migration towards the sample parts close to the cooling plate where freezing occurred. Due to the low number of samples, we cannot quantify saturation effects on frost weathering, however, our set up enables us to incorporate the variability of saturation levels occurring in natural rockwalls and to test the consistency of frost damage patterns.

To monitor acoustic emission (AE) which are used as a proxy for cracking (Eppes et al., 2016; Hallet et al., 1991), a Physical Acoustics AE sensor PK6I with a frequency between 35 and 65 kHz was mounted with acrylic sealant on top of each rock sample. (Fig. 1a). The detected AE signals were recorded with a Physical Acoustics micro SHM node. Recorded data were subsequently processed and filtered using Physical Acoustics AEWin software. ~~We used~~Due to low background noises of our setup, we set an initial signal threshold of 30 dB_{AE}, which is similar to Mayer et al. (2023) ~~and who established a threshold of 35 dB_{AE}~~, due to the presence of stronger background noises. We performed lead break tests as sample cracks (Eppes et al., 2016) ~~to evaluate~~ before and after each scan to control sensor coupling and evaluating system performance and wavelength form ~~and test the setup. To prevent false~~. Poor coupling of an AE sensor could lead to diminished AE amplitudes, meaning signals of low amplitude might not be detected by the system. To avoid erroneous AE signals stemming from the setup itself ~~we tested~~, the system ~~by running~~underwent testing without any freezing or ~~changing the~~ temperature alterations.

During freezing test 1 (FT-1), we simulated diurnal freeze-thaw conditions and exposed three samples with different saturation levels (Fig. 1b) to 20 freeze-thaw cycles (Fig. 1c). In each cycle, we cooled down the samples until the cooling plate reached -20 °C and the rock temperature at the bottom of the samples was approximately -10 °C followed by one hour warming until a cooling plate temperature of 5 °C and sample temperatures between 5 and 7°C were achieved. Small sample temperature deviations could occur due to thermistor placement at the side of the sample or ice development between cooling plate and rock samples. Our set up enabled us to develop a thermal gradient within the samples (Fig. 1d) where the lower part of the rock samples between 0 and 40 mm sample height including the scanned area between 5 mm and 19 mm sample height (Fig. 2a) were exposed to freezing conditions while the upper parts remain unfrozen. The freezing rate we utilized, 12.5°C per hour at the cooling plate, might surpass those observed in natural rockwall settings, yet it is comparable to the rates employed in earlier freezing studies (Jia et al., 2015; Matsuoka, 1990). The applied freezing rate could amplify frost cracking and result in an overestimation of frost damage.

In our second experiment, we subjected three rock samples, each with varying levels of saturation (Fig. 1b), to an extended period of freezing (FT-2), maintaining the cooling plate at -20 °C for 68 hours. This setup resulted in a temperature gradient within the samples, with the lower 0-40 mm of the samples experiencing freezing temperatures and the upper section remaining above freezing, maintaining a stable thermal gradient for about 66 hours (Fig. 1d). The setup aimed to enable the migration of water from the unfrozen segment to the frozen one enhancing the potential for frost cracking; however, the sample's low porosity combined with the small size of the unfrozen segment limits the amount of water that can migrate, potentially resulting in an underestimation of frost damage compared to what might be observed in natural conditions.

2.3 μ CT imaging

In order to identify crack locations and quantify crack growth, X-ray computed micro-tomography (μ CT) was performed at the Ghent University Centre for Tomography (UGCT) with the CoreTom (TESCAN XRE) μ CT scanner. ~~Only the bottom part (0–20 mm) of the sample was scanned, since only this part experienced sub-zero temperatures (Fig. 3b).~~ For experiment FT-1, μ CT scans were performed before the start and after every five cycles (Fig. 43). For the sustained freezing experiment (FT-2), rock samples were scanned before and after the experiment. As only the bottom part of the sample (0–40 mm) experiences freezing (Fig. 1c-d), the rock sample sections between 0 and 20 mm were scanned (Fig. 2a). The dimension of the section was determined to optimize the resolution, as the resolution of scanning is influenced by the size of the sample (Cnudde and Boone, 2013). The μ CT system settings for our experiment were set to 179 kV for the X-ray source with a power output of 20 W. The scans were performed at binning 2 and a voxel size of 20 μ m. A ~~1~~ one mm thick aluminium plate was used to filter low energy X-rays and reduce beam hardening. For each sample 2142 projections were made with an exposure time of 600 ms. The raw μ CT data was reconstructed using the software PANTHERA (TESCAN XRE) where beam hardening and ring filters were applied, and which resulted in a stack of cross-sections saved as 16-bit tiff. Images. All subsequent image handling, such as registration, segmentation, and analyses, were performed with Avizo3D Pro (Version 2021.1, ThermoFisher Scientific). In Avizo, a sandbox filter was conducted to bin contrast variations inside the images and match contrast between the single scans. We tuned the parameters until visually the best result was observed. Therefore, sample voids (pore space) and matrix (sample material) of each image could be separated by thresholding over contrast. We followed the work after Deprez et al. (2020a) and defined a distinguishable feature in the scan image as a minimum spatial resolution of 3 times the voxel size (60 μ m). Volume fractions and the expansion of pore space in the sample were ~~determined~~ assessed using photogrammetry in Avizo. For each image ~~by calculating differences, the software detected and quantified distinctions~~ between ~~voids~~ void voxel V_V and the matrix voxel V_M , which we used for later comparison call crack fraction cf (Fig. 2b). Crack fraction is derived by:

$$cf = \frac{V_V}{V_V + V_M} \quad (1)$$

This approach enabled subsequent comparisons between ~~the~~ scans to ~~evaluate~~ assess the development of pore space growth in the sample (Fig. 2c,d). The parameter crack ~~volume~~ fraction was defined by the total amount of segmented pore space (voids) per image in the image stack (cross section) divided by the total amount of segmented sample material (matrix + voids). Due to effects of beam hardening ~~effects~~, which result in image distortion at sample heights between 0 and 5 mm as well as and between 19 and 20 mm, our analyses were concentrated on the portion of the rock sample height (ranging from the bottom), we focussed in our analyses on 5 to 19 mm in height of our rock sample. We quantified crack growth (pore space growth) by comparing the crack ~~volume~~ fraction per layer after each scan (Fig. 2d and 6a-f). ~~Potential influences of initial varying crack density were evaluated by normalizing each sample scan with its own initial crack volume (Fig. 6g-i).~~ If growth occurs in every crack or void, this implies that the distribution of initial cracks/voids could either accelerate or decelerate the growth of cracks. Consequently, crack growth cannot be directly compared across samples due to variations in crack distribution. To address this, we adjusted each scan cf_i by its initial crack fraction cf_0 , allowing for an assessment of

crack growth that is independent of the initial crack distribution. The normalized crack fraction, cf_{norm} , for each scan is calculated as follows:

$$cf_{norm,i} = \frac{cf_i}{cf_0} \quad (2)$$

where i represents the scan number. For the purpose of assessing the progression of quantified frost damage both within a single sample and among different samples, we computed the mean of cf_{norm} for each scan.

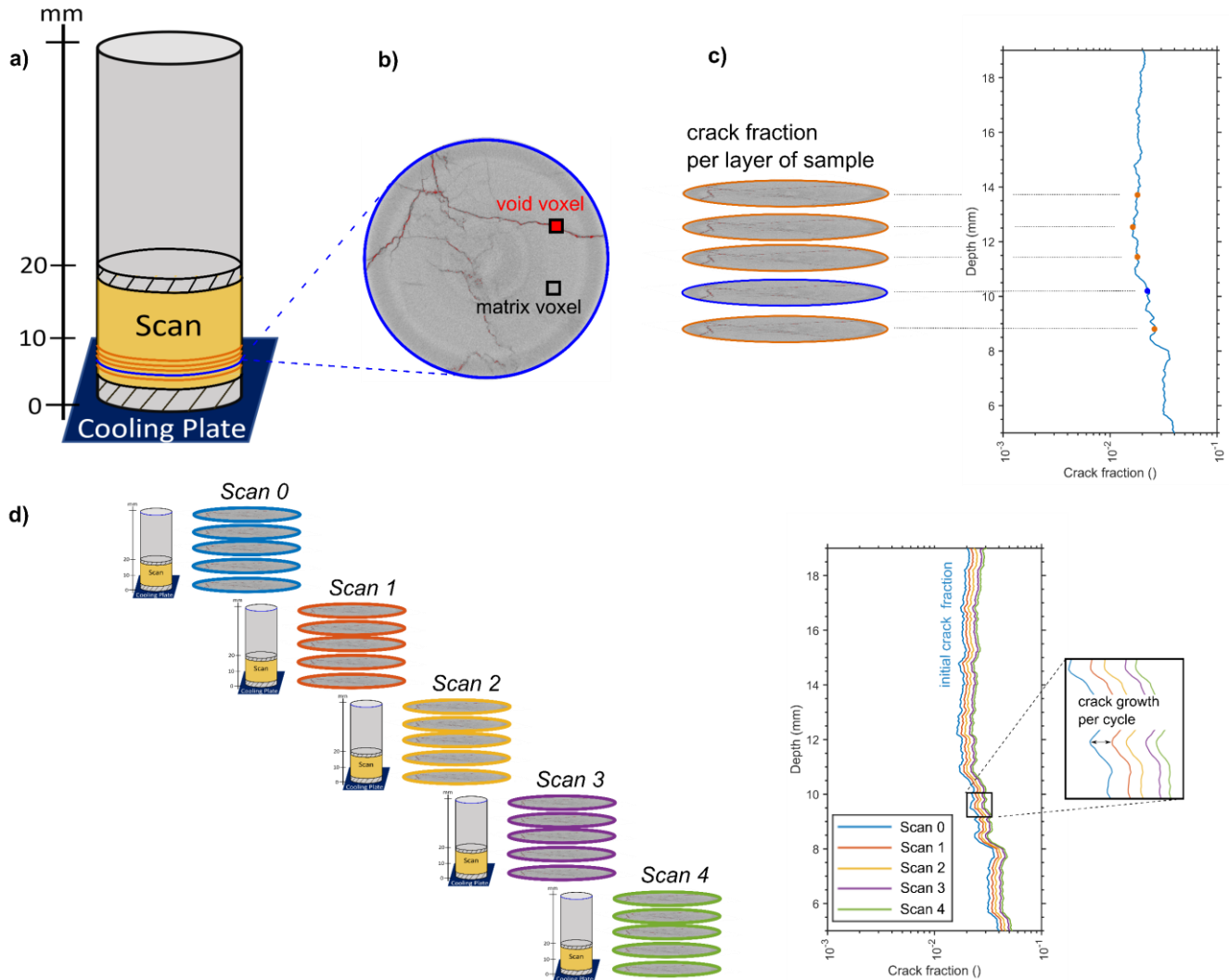


Figure 2: Schematic drawing from scan to crack growth. a) scanned volume from 0 – 20 mm sample height. Due to beam hardening effects (black dashed area) at the edges only the area between 5 - 19 mm sample height was analysed. b) Example scan of one layer (20 μ m thick) with example void/crack voxel and matrix voxel derived by Avizio3D Pro. c) Crack fraction derived for each layer

275 [over the whole scanned height from 5 - 19 mm by photogrammetry. d\) Example of resulting crack growth per cycle with initial crack fraction \(blue line\).](#)

2.4 Thermal- and ice-stress modelling

We modelled thermal and ice stresses to determine potential drivers of AE signals and porosity growth. The models require a one-dimensional temperature distribution inside the samples. Temperature distributions were calculated by assuming a linear and homogeneous temperature gradient between all temperature sensors (Fig. [3b1d,e](#)). Latent heat effects were incorporated in general as our sensors measured rock temperatures which were affected by latent heat effects. All thermal and ice stress simulations were performed in MATLAB (2021). Thermal stress occurred in our samples as a result of changing temperatures. We modelled one-dimensional thermal stress σ_{TL} after Paul (1991):

$$\sigma_{TL}(t) = 2 \cdot G \cdot \alpha_T \left| \frac{dT_{L\pm 5}}{dt} \right| (1 + \nu), \quad (43)$$

285 with thermal expansion coefficient α_T , shear modulus G and Poisson ratio ν (Table 1). $T_{L\pm 5}$ represents a running temperature mean over five minutes. Our model approach did not incorporate complex crack geometries of the samples; therefore, we could only provide quantitative estimates of thermal stress. Hence, we focused in our analysis on timing of thermal stresses and did not analyse absolute stress values.

We applied frost cracking modelling to determine ~~the time dependency of when~~ ice stresses [occur](#) during the ~~testtests~~. Frost cracking modelling was performed using the model of Walder and Hallet (1985), which combines hydraulic and mechanic rock properties. The model simulated ice pressures in a single 1 mm long mode I crack. Therefore, this model simplified crack geometry and provided quantitative estimates of ice pressures. Due to the abstract model predictions, we used quantified ice pressures only to interpret [the](#) timing of AE events and not ~~as absolute values.~~

295 [to relate ice pressure to rock damage. We will test different parameter influences on model prediction in a sensitivity analyses \(see Fig. S1 and S2 in Supplementary Information\).](#) The basic model requirement to start ice segregation are rock temperatures below the pore freezing point T_f and an unfrozen area inside the rock, which acts as a water reservoir- ([Fig. 1d](#)). The transition area ~~in~~ between a potential ice lens in the frozen part and the unfrozen area is called frozen fringe. The model assumes a fully saturated rock. Ice pressure rises between lens and pore/crack wall when water migration is driven by a thermodynamic potential gradient through the frozen fringe. The amount of supplied water is governed by Darcy's law but restrained due to hydraulic conductivity inside the frozen fringe and flow resistance due to the thin film between ice and crack wall.

305 Following Walder and Hallet (1985), we chose a hydraulic conductivity of k_{hc} of $5 \times 10^{-14} \text{ m s}^{-1}$. Flow resistance between the ice and pore wall depends on grain size R , liquid-layer thickness h_l , and ice-free porosity n_f . Walder and Hallet (1985) set the grain size to 0.75 mm, the liquid-layer thickness to $6 \text{ nm } ^\circ\text{C}^{1/2}$ (after Gilpin (1980) at a temperature of $-1 \text{ }^\circ\text{C}$) and neglected ice-free porosity. A simplified potential ice lens has the form of a penny-shaped crack with a crack radius c and a width w .

Table 1. Parameters used for thermal stress and frost cracking modelling of Dachstein Limestone samples.

Parameter		Value
Ice density (kg m ⁻³)	ρ_i	920
Water density (kg m ⁻³)	ρ_w	1000
Pore freezing point (°C)*	T_f	-1
Hydraulic conductivity (m s ⁻¹)*	k_{hc}	5×10^{-14}
Grain size (mm)*	R	0.75
Liquid layer thickness (nm °C ^{1/2})*	h_l	6
Initial crack length (mm)*	x_i	1,20,40
Angle between crack plane and rock wall (°)*	ϕ	0
Poisson' ratio ()	ν	0.327 ± 0.033
Critical fracture toughness (MPa m ^{1/2})	K_C	1.32 ± 0.13
Growth-law parameter (m s ⁻¹)*	V_c	340 ± 34
Growth-law parameter (*)	γ	37.1 ± 3.7
Rock density (kg m ⁻³)	ρ_r	2690
Rock porosity (%)	n_r	0.1
Shear modulus (GPa)	G	24.02 ± 2.4
Young's modulus (GPa)	E	63.74
Thermal expansion coefficient (°C ⁻¹) ⁺	α_T	6×10^{-6}

* Walder and Hallet (1985), ⁺Pei et al. (2016)

330

3 Results

3.1 Results of Continuous AE logger and simulation temperature monitoring and stress modelling

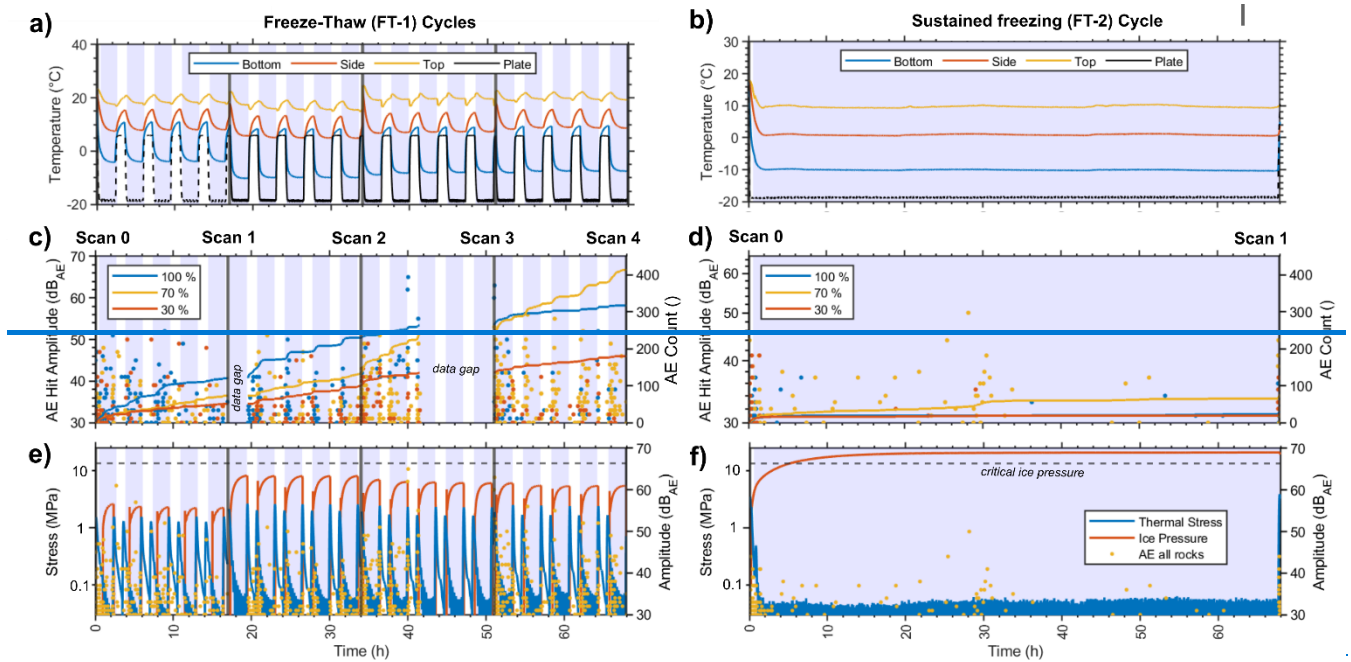
3.1.1 Freeze-Thaw cycles (FT-1)

335 ~~The cooling plate exposed the bottom of~~ The rock ~~samples~~ samples' bottom was exposed to temperatures oscillating between
a temperature range of -19 and to 6 °C. ~~The~~ by the cooling plate. Initial temperature loggers ~~between scan 0 and 1~~ were poorly
~~coupled/attached~~ to the rock, ~~which led to an offset between rock~~ causing discrepancies in bottom surface temperatures ~~at the~~
~~bottom between freeze thaw cycles 1-5 compared to temperatures between freeze thaw cycles 5-20 (Fig. 4a).~~ The temperature
~~sensor on the cooling plate was added after~~ during the first five freeze-thaw cycles (Fig. 4a) ~~compared to later cycles, as shown~~
340 in Fig. 3a, suggesting that the actual temperatures were likely lower than those recorded. After five cycles, a temperature sensor
was added to the cooling plate. Between freeze-thaw cycles 5 and 20 the bottom rock temperature reached minimal
temperatures of -10 to -8 °C and maxima of 8.5 to 9.5 °C. ~~The upper temperature, while the top sensor showed overall positive~~
~~temperatures varying between~~ consistently registered 15 and to 24 °C. ~~We detected~~ 317
345 More AE hits in the 100 % sample, 415 in the 70 % sample and 180 in the 30 % sample (Fig. 4e), were recorded during
freezing phases ~~more AE hits were detected~~ compared to non-freezing ~~phases.~~ Most ones (Fig. 3c). ~~The majority of the~~ hits
~~were detected/occurred~~ when ~~the bottom sensor showed~~ temperatures were below ~~the freezing point,~~ with the highly saturated
sample registering 235 hits ~~for,~~ the fully/partly saturated sample, 326 hits, and the low saturated sample 123 hits. Positive

350 temperature readings yielded fewer hits: 82 for the highly saturated, 89 for the partly saturated, and 423 hits 57 for the low saturated sample. When the bottom sensor measured positive temperatures, we recorded 82 hits at the 100 % rock, 89 hits at the 70 % rock and 57 hits samples. Total AE hits observed were 317 for the 30 % rock. The AE logger system stopped recording twice, between 17-19.5 h and 41.5-51 h, therefore, we underestimate the number of accumulated hits for the FT-1 cycle. Most AE hits were measured between scan 0 and 1 with a maximum of 121 hits highly saturated sample, 415 for the partly saturated sample, and 180 for the 100 % low saturated sample, followed by 73.

355 Throughout the cycles, a pattern of accumulating AE hits for the 70 % and 51 hits for among the 30 % samples is evident. Initially, the highly saturated rock sample. In the last period between scan 3 and 4, the 70 % accumulated the majority of hits in the first 10 cycles (121 hits). However, there was a notable increase in AE hits for the partly saturated sample showed the highest AE accumulation with, eventually leading to a higher total than the highly saturated sample between 10 and 20 cycles (173 hits, while sample 100 % had 53 hits and the 30 % only 44 hits.). Given the consistent trend observed in both the highly and low saturated samples, a likely shift in the coupling between the AE sensor and the sample is suggested. Consequently, it

360 is probable that the total AE hits for the partly saturated sample were fewer than those for the highly saturated one. Due to two recording interruptions of the AE logger, AE hits for the FT-1 cycle are likely underestimated.



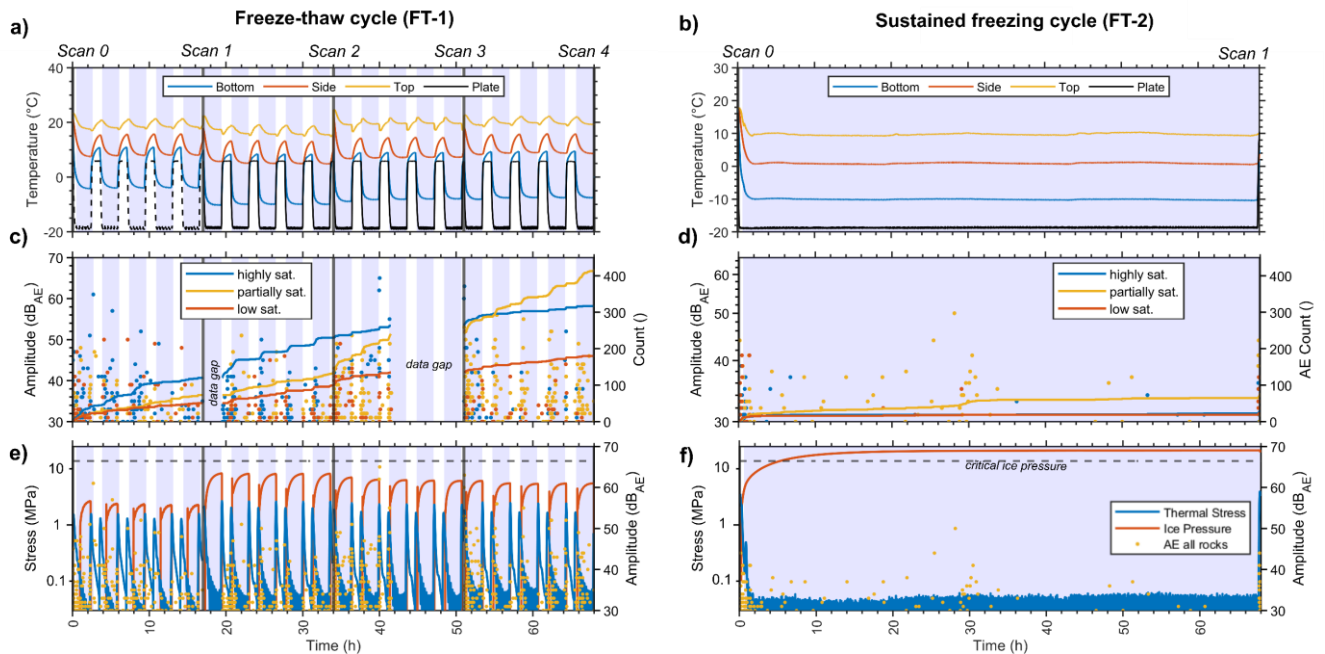


Figure 4.3: FT-1 resulted in significantly more AE hits than FT-2, as indicated by thermal stress models but not reflected in frost cracking models where FT-2 showed higher predicted ice stresses. More AE hits were recorded during freezing phases compared to non-freezing ones. a-b) Respectively measured rock and cooling plate temperatures, c-d) recorded AE hits (coloured dots) and cumulative AE hits (coloured lines), and e-f) modelled thermal and ice stresses at bottom temperature sensor plotted against time for FT-1 and FT-2 with AE hits from all samples. The dashed black line highlights cooling plate temperatures according to the controller while black lines indicated measured plate temperature. (cooling plate sensor was attached after first 5 cycles). The temperature offset between scan 0 and 1 during FT-1 (a) is a result of poor connectivity of the bottom temperature sensor. Blue rectangles highlight periods when bottom rock samples were exposed to temperatures below 0 °C.

Our modelling yielded a maximum occurrence of model indicated that both thermal- and ice-induced stresses peaked during freezing temperatures (Fig. 4e). However, due to a temperature offset between discrepancy in the initial five freeze-thaw cycles 1-5 resulted in an underestimation of, the modelled thermal and ice stresses stress were underestimated (Fig. 4e). During freeze-thaw 3e). From the fifth to the twentieth cycle 5 to cycle 20, peak, the highest thermal stresses increased when temperature shifted occurred as temperatures transitioned from thawing to freezing conditions with resulting, reaching pressures of 2.15 ± 0.25 MPa and 2.95 ± 0.20 MPa from freezing to thawing, respectively. These stresses were minimal at stable temperatures, thermal stress reached its minimum. Ice stress was present only occurred during freezing phases. Inside the freezing regime, with the model predicted rising predicting increasing ice stresses with up to a maximum of 6.85 ± 1.35 MPa at the end of each freezing phase, which. This is far significantly below threshold for the critical ice pressure threshold (13.7 MPa) that can be referred to for subcritical cracking.

3.1.2 Sustained freezing cycle (FT-2)

In the FT-2 run, the partially saturated sample registered the highest number of AE hits, with ice stresses being a major factor. The rock samples were exposed to/underwent 68 hours of freezing conditions for 68 h with 66 h being at a fixed, maintaining a constant bottom rock temperature of -10 ± 0.5 °C (Fig. 4b 3b). During fixed temperature conditions this period, the middle temperature sensor stayed at/recorded a slightly positive temperature/temperature of 0.9 ± 0.3 °C, and the top sensor stayed at 9.8 ± 0.4 °C. Our AE loggers detected/logging revealed 28 hits at/for the 100 %/highly saturated, 77 hits at/for the 70 %/partially saturated, and 23 hits at/for the 30 %/low saturated rock sample (Fig. 4d 3d). The fixed freezing phase caused 11 hits to occur at the fully/highly saturated rock, 53 hits at the partly saturated rock and 8 hits at the low saturated rock. Thermal stress modelling predicted/indicated peak values/stresses of 3.6 MPa for/during cooling and 3.9 MPa for/during warming at the beginning/cycle's start and end of the freezing cycle (Fig. 4f). During fixed temperatures thermal stress stayed 3f), dropping below 0.1 MPa— at stable temperatures. Ice stress models showed a continuous increase in ice stress throughout the freezing phase—the ice stress model predicted a rising ice stress with, reaching a maximum of 21 MPa. Ice pressure exceeded, surpassing the critical ice pressure threshold of 13.7 MPa after 5.4 h.—hours.

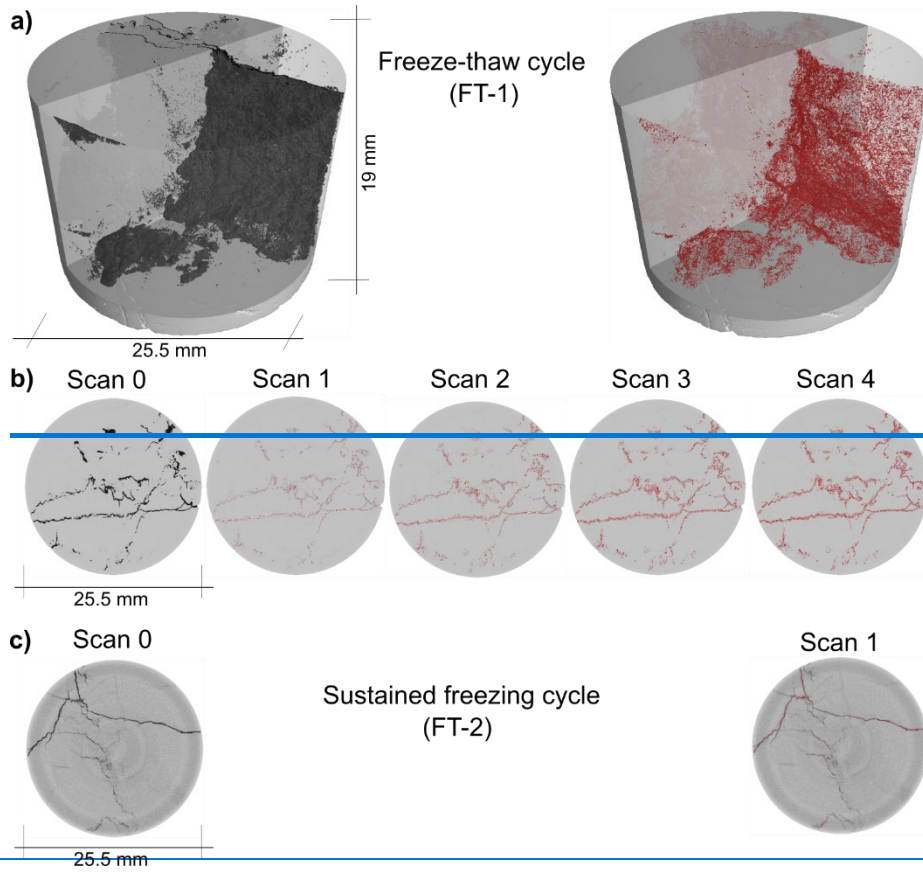
3.2 Results of Discontinuous μ CT monitoring

3.2.1 Freeze-Thaw cycles (FT-1)

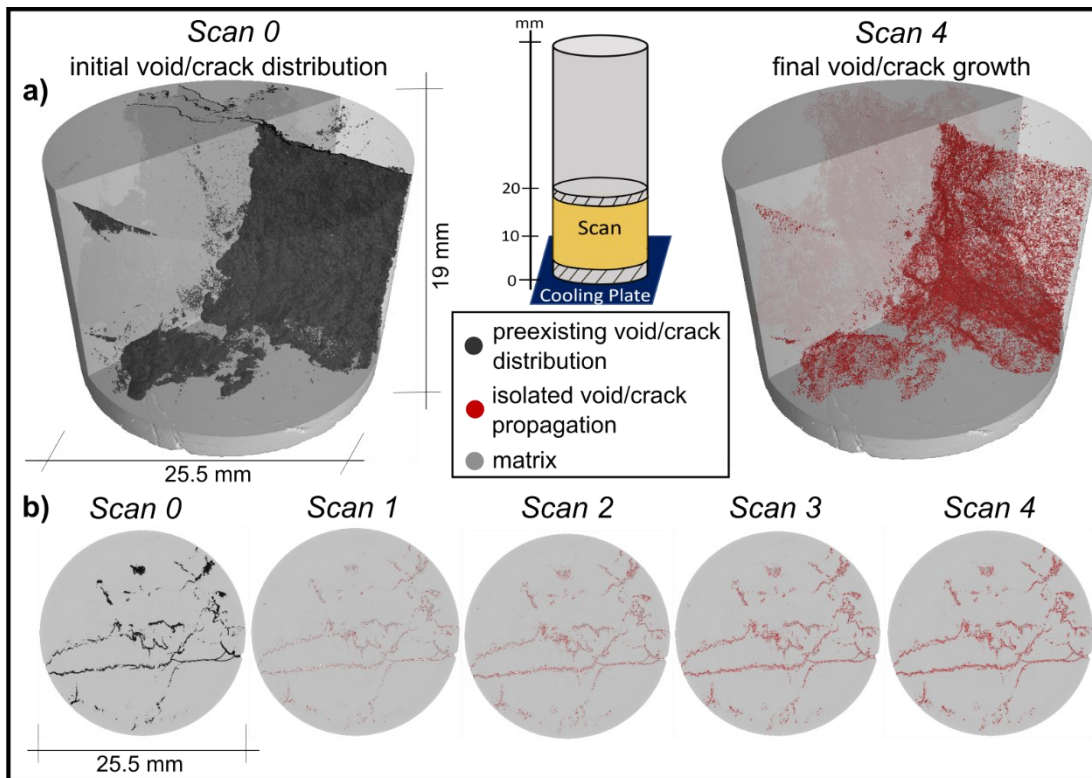
As the experiments were executed/Conducted with a spatial resolution of 60 μ m, the μ CT scans show/indicated that most/the majority of the pore volume in our samples are/consisted of cracks—and that volume—, with changes occur—in form of volume manifesting as crack growth/expansion (Fig. 5 4). The data revealed that crack growth was independent of expansion of cracks was found to be consistent throughout the height in/of the sample, however, crack growth revealed a positive correlation/indicating that the growth of cracks was uniform from the topmost scanned section (19 mm) to the lowest (5 mm). However, there was a discernible positive relationship between initial crack volume and subsequent crack growth (Fig. 6a 5a-c). The initial/Crack fraction of crack volume (volume of crack divided by total volume) per layer from in the initial scan (scan 0) before freezing varied between 0.014—0.042 for the 30 % rock, 0.003—0.011 for the 70 % rock and 0.005—0.012 for the 100 % rock. The crack volume increased uniformly/independently/exhibited variations from height at all tests.— $0.023^{+0.019}_{-0.009}$ in the low saturated rock, $0.006^{+0.005}_{-0.002}$ in the partially saturated rock, and $0.007^{+0.005}_{-0.002}$ in the highly saturated rock. The final (scan 4) crack fraction was $0.031^{+0.028}_{-0.009}$ (an increase of 35 %) for the low saturated rock, $0.008^{+0.006}_{-0.004}$ (an increase of 33 %) for the partially saturated rock, $0.011^{+0.006}_{-0.003}$ (an increase of 51 %) for the highly saturated sample.

To exclude/mitigate the sensitivity/influence of crack growths to initial crack distribution on crack growth analysis, we normalized the growth of crack volume growth—for each sample by/relative to its initial crack volume. Normalization

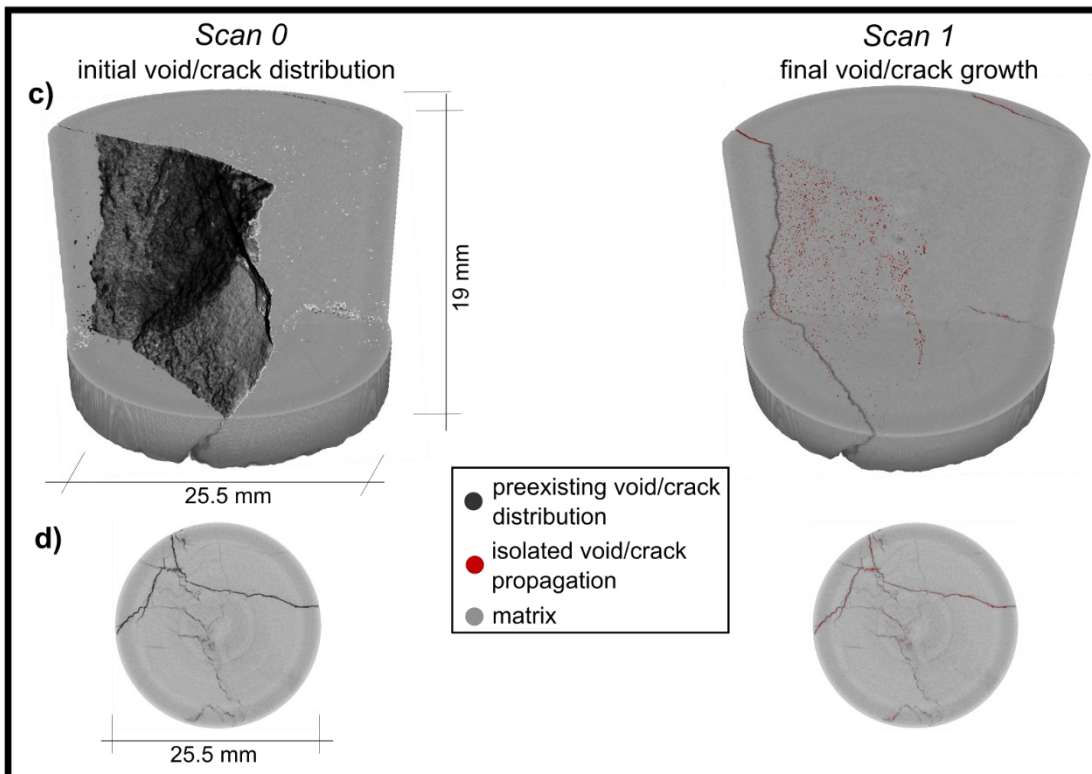
revealed fraction (see Eq. 2). This normalization showed that crack ~~volume~~ growth was ~~not dependent over~~ consistent throughout the ~~sample's~~ height, though the extent of the ~~samples, however, the amount of crack volume~~ growth per scan ~~varies~~ varied with saturation levels (Fig. 6g5g-i). For the whole experiment, the final Scan 4 ~~showed~~ revealed a final mean normalized crack growth of 1.34 ± 0.8 (~~i.e. equivalent to 34% more crack volume than initially~~ the initial value) for the ~~30%~~ low saturated sample, 1.29 ± 0.11 (~~i.e. 29% more crack volume than initially~~ increase) for the ~~70%~~ partially saturated sample, and 1.52 ± 0.13 (~~i.e. 52% more crack volume than initially~~ increase) for the ~~fully~~ highly saturated sample. The average mean normalized ~~growth of~~ increase in crack volume ~~in~~ between scans was 0.8 ± 0.03 (~~i.e. 8% more crack volume than initially~~ increase) for the ~~30% rock, low saturated sample,~~ 0.07 ± 0.04 (~~i.e. 7% more crack volume than initially~~ increase) for the ~~70% rock~~ partially saturated sample, and 0.13 ± 0.05 (~~i.e. 13% more crack volume than initially~~ increase) for the ~~100% rock,~~ highly saturated sample.

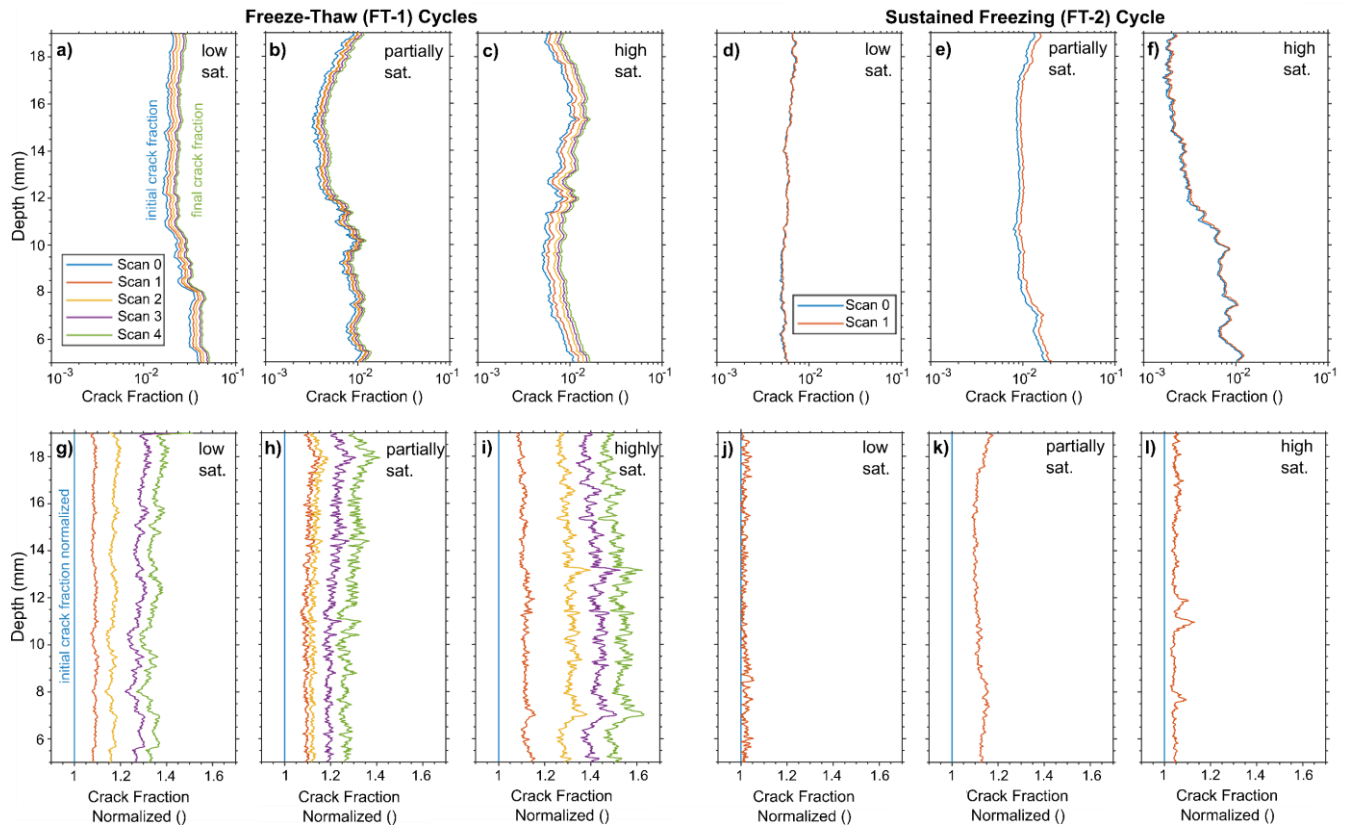


Freeze-thaw cycle
(FT-1)



Sustained freezing cycle
(FT-2)





450 **Figure 5: μ CT effectively showcases the progression of cracks in our samples, illustrating a steady growth in crack volume that is uniform throughout different heights in the sample and directly correlates with the initial crack volume.** a-f) Measured crack volume fraction (volume of cracks/voids divided by total volume, refer to Fig. 2b) using μ CT plotted against rock depth. g-l) Quantified normalized crack volume fraction by initial crack volume (blue line a-f) plotted against rock depth.

3.2.2 Sustained freezing cycle (FT-2)

455 ~~The sustained~~During the prolonged freezing experiment ~~revealed that~~, the ~~highest~~most significant crack volume growth ~~occurred~~was observed in the ~~70%~~partially saturated rock sample, followed by the ~~fully~~highly saturated rock sample, ~~while one~~. In contrast, the ~~30%~~low saturated rock sample ~~showed almost no~~exhibited minimal crack growth (Fig. ~~6d~~5d-f). Scan 0 showed ~~an~~The initial crack volume fraction ~~between~~at scan 0 ~~0.005–0.008~~ ranged from $0.005^{+0.006}_{-0.003}$ for the ~~30%~~low saturated rock, $0.008^{+0.008}_{-0.002}$ for the ~~70%~~partially saturated sample, and $0.001^{+0.006}_{-0.001}$ for the ~~fully~~saturated rock. Normalization revealed the ~~highest~~highly saturated sample. The final crack fraction was $0.005^{+0.007}_{-0.003}$ (an increase of 0 %) for the low saturated sample, $0.012^{+0.008}_{-0.003}$ (an increase of 17 %) for the partially saturated rock, $0.006^{+0.001}_{-0.001}$ (an increase of 0 %)

460 Normalized data indicated the most pronounced crack growth ~~at~~in the ~~partly~~partially saturated sample (Fig. ~~6j~~5j-l). We ~~calculated~~The final scan revealed a mean normalized crack growth ~~for the 30% rock with~~as 1.02 ± 0.02 (i.e. indicating a 2%

465 ~~more% increase in crack volume than initially),) for the 70 % rock with low saturated sample, 1.12 ± 0.04 (i.e. 12 % more crack volume than initially),% increase) for the partially saturated sample, and for the 100 % rock with 1.05 ± 0.03 (i.e. 5 % more crack volume than initially),-% increase) for the highly saturated sample.~~

4 Discussion

470 4.1 ~~CT~~ Critical discussion on AE Monitoring, stress modelling and μ CT technique

Thermal and ice stresses or a combination of these stresses can cause rock damage. We monitored AE as a proxy for cracking as previous stress experiments (Eppes et al., 2016; Hallet et al., 1991) and analysed the timing of AE events in combination with simplified thermal stress and ice stress models to decipher the potential stress source. Our findings indicate a proportional relationship between the number of AE events and rock damage quantified via μ CT (Fig. 6a,d) which was also shown by findings of Wang et al. (2020a) and. However, in our study the highest count of AE hits does not always align with the most visible rock damage (Fig. 6a). Specifically, the partially saturated sample exhibited over 415 AE hits with a normalized crack growth fraction of 47%, while the low saturated sample displayed 180 AE hits alongside a 53% crack growth. In contrast to our setup, Wang et al. (2020a) ~~history~~ utilized a rock sample with artificially created macro fractures that predominantly drove the generation of AE signals. The discrepancy in our results might be due to variations in volume growth per crack propagation, potentially causing fewer AE releases with greater porosity growth. Additionally, the distinct responses of our natural rock samples to stress, influenced by slightly varying rock parameters, crack distribution and saturation, could also impact the number of AE hits. A potential alteration in the AE sensor's attachment to the rock might affect also signal detection. Although we reattached sensors and conducted lead break tests during the FT-1 cycle, the connection could have changed over time. Given the consistent AE accumulation trend observed in both the highly and low saturated samples, a likely coupling shift at the partially saturated sample is suggested (Fig. 3e), which was not reflected in μ CT crack growth data (Fig. 5b, h). Despite these variables, the partially saturated sample showed before the shift already a higher AE accumulation than the less saturated one, underscoring that AE hits did not completely correlate with crack growth.

Our approach to model thermal stress did not account for the complex geometries of the cracks in the samples. As a result, our analysis concentrated on the timing of thermal stresses rather than their precise magnitudes. In our frost cracking modelling, we presented results for ellipsoidal cracks starting at a length of 1 mm. It is important to note, however, that cracks vary in size and exhibit more intricate geometries as seen by μ CT imaging (Fig. 4). Additionally, slight variations in mechanical and elastic properties may occur since parameters were derived from different boulders of the same lithology or were based on data from Walder and Hallet (1985). Our sensitivity analysis (see Supplementary S1 and S2) for frost cracking models revealed that the timing of increasing ice pressure was largely consistent across variations in parameters such as fracture toughness, growth law parameters, shear modulus, and Poisson's ratio. Nevertheless, the crack length significantly influences the timing

and the critical threshold for cracking. A larger crack length results in lower and delayed ice stresses, as well as a reduced critical threshold.

Prior μ CT measurements have demonstrated the capability to quantify crack growth, as illustrated by Deprez et al. (2020b) in their study on highly porous (30-40%) oolitic limestone building stone, and by De Kock et al. (2015) in their examination of highly porous (~35%) miliolid limestone. These studies revealed the microscopic activities taking place within limestone pores throughout freeze-thaw cycles. The authors linked the pore processes to potential patterns of macroscopic damage. In their experiments, both groups worked with small samples measuring 8-9 mm in diameter, achieving resolutions of 21 μ m (Deprez et al., 2020b) and 20.4 μ m (De Kock et al., 2015), respectively. In contrast, aiming to create a thermal gradient and water movement, we utilized larger samples, which led to a reduced spatial resolution of 60 μ m. Our experiments demonstrated our capability to visualize and quantify damage in low-porosity rock samples caused by freeze-thaw cycles, while also acknowledging the possibility of minor additional damage not detectable by μ CT resolution. Previous laboratory freeze-thaw tests have used a decrease in elastic properties such as P-wave velocity, Young's modulus or increases in porosity (Whalley et al., 2004; Matsuoka, 1990; Draebing and Krautblatter, 2012) as a proxy for frost damage. Yet, detecting frost damage in low-porosity alpine rocks poses challenges due to the minimal or undetectable alterations in these elastic properties or porosity levels. Moreover, the use of measured elastic properties or porosities does not provide information on crack geometry and crack growth. We demonstrated that cracks grow along pre-existing cracks and highlighted that μ CT is a powerful analytical tool.

4.2 Influence of initial cracks on crack growth

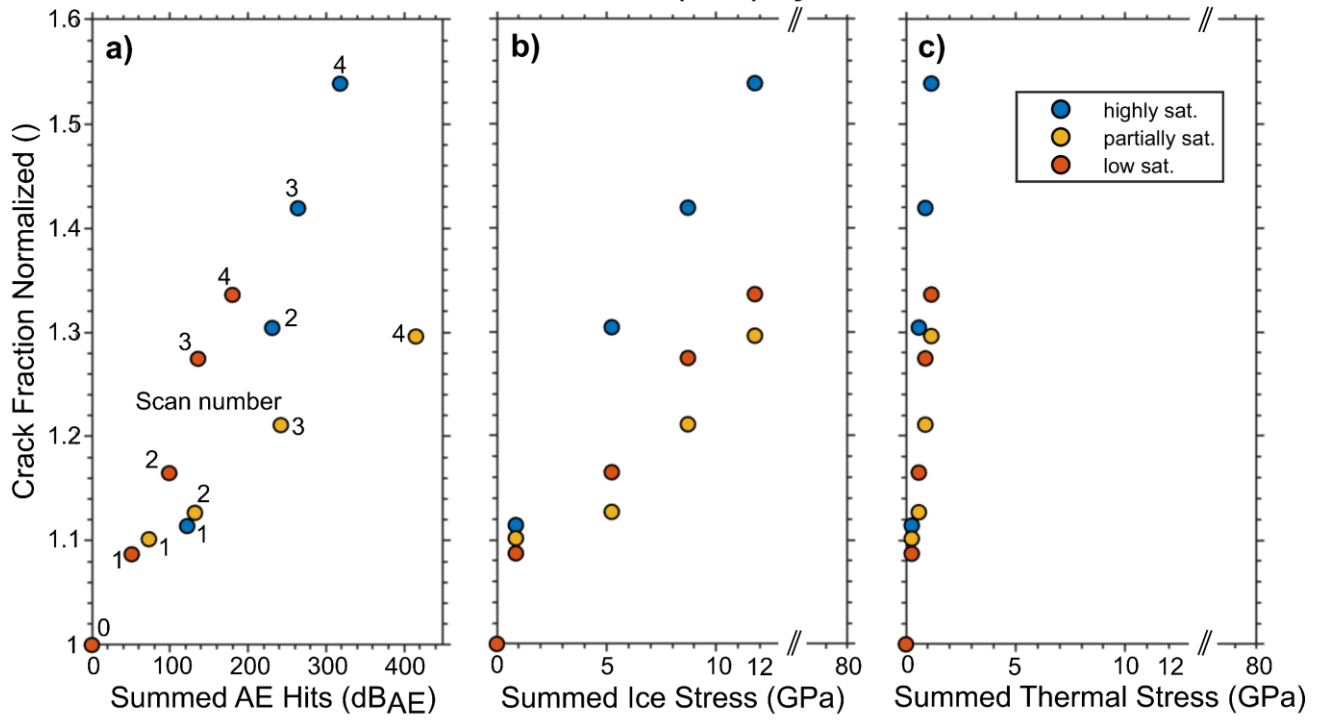
In alpine rocks, freezing leads to causes expansion in the pore space growth spaces along pre-existing cracks, which is influenced by the initial crack density. Our normalised μ CT results revealed of these cracks. Although our samples were extracted from the same boulder and appeared to have a uniform distribution of cracks visually, μ CT scanning revealed differences in the internal distribution of cracks across the samples. Our normalized μ CT findings show a consistent increase in pore space growth along the depth of the sample expansion across the height of the samples, evident across pre-existing cracks through both freeze-thaw cycles. This uniform pattern suggests an influence of crack density indicates that the density of cracks plays a role in the extent of crack growth expansion, with increased a notable increase in crack growth due linked to higher initial crack densities of cracks or initial pore volume (volumes, as shown in Fig. 6g-i). This finding is supported highlighted by the scan visualization images (Fig. 54), which highlights predominantly display the expansion of pore space growth mainly in spaces within pre-existing cracks, as captured within the resolution of μ CT. Our results are consistent findings align with theoretical assumptions models proposed by Scherer (1999) and Walder and Hallet (1985) or, which suggest that ice crystallisation crystallization pressure increases escalates in pore spaces, which potentially leading to the enlargement of pores or cracks. This is supported further corroborated by microscopic findings analyses by Gerber et al. (2022), who confirmed that such pressure could indeed facilitate pore or crack expansion. Wang et al. (2020b), utilizing μ CT with a 35 μ m resolution, found that pore space expansion in granite occurred exclusively as propagation of artificial created cracks.

530 without evidence of new crack formation. Similarly, Dewanckele et al. (2013) that can lead to pore or crack growth. Previous
 μ CT measurements on highly porous (30-40 %) oolitic limestone building stone by or highly porous (~35 %) miliolid
limestone by showed the microscopic processes occurring in limestone pores during freeze-thaw cycles. The authors were
able to relate the pore processes to possible macroscopic damage patterns. Both experiments used small samples with 8-9 mm
535 in diameter, allowing a resolution of 21 μ m and 20.4 μ m. As we aimed to generate a thermal gradient and water migration,
we used larger samples resulting in a lower spatial resolution of 60 μ m observed no new crack formation within the rock matrix
through μ CT imaging at a 2.5 μ m resolution in high-porosity Lede and Noyant limestones, pinpointing that pore space growth
transpires at pre-existing weak zones (such as fossils). We state that most frost damage occurs in preexisting cracks or voids
and lead to crack propagation or widening with the process intensifying as crack density increases.

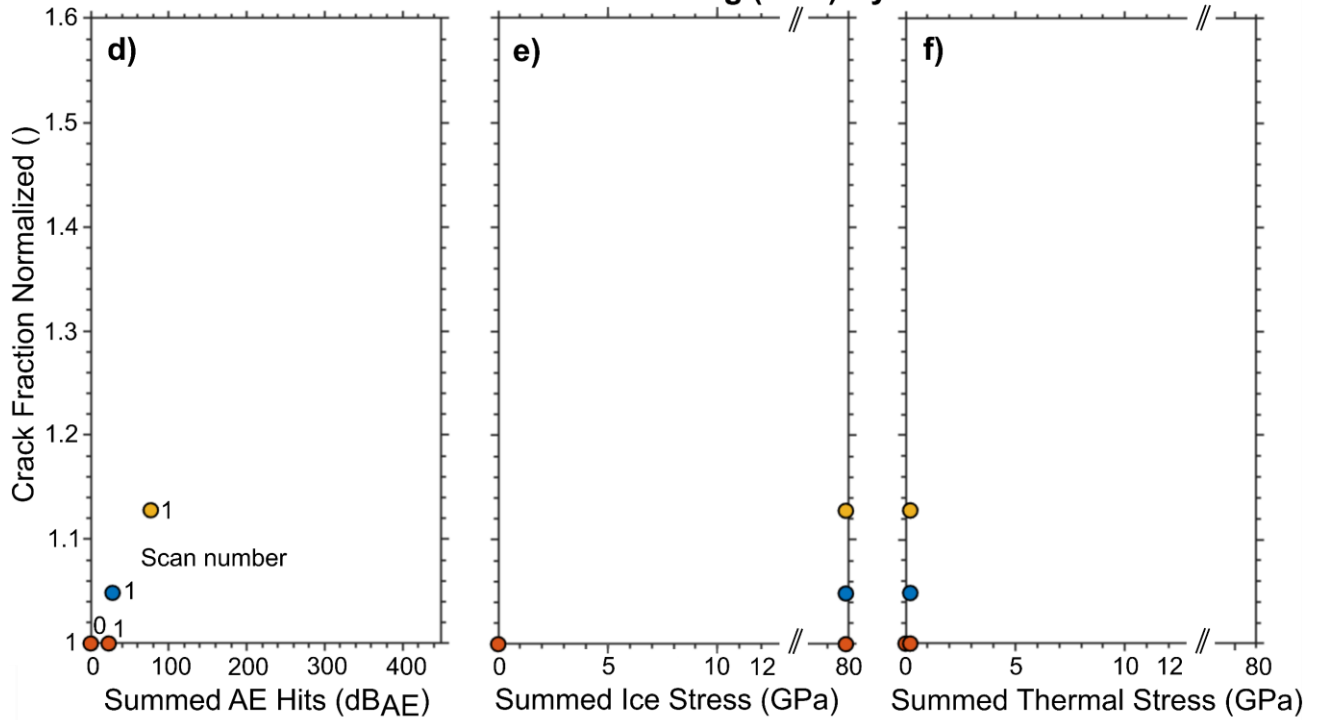
540 **4.3 Efficacy of freeze-thaw and sustained freezing cycles**

Based on μ CT data, freeze-thaw cycles (FT-1) revealed higher rock damage compared to a sustained freezing-cycle (FT-2) in
low-porosity crack-dominated alpine rocks. Final crack growth is affected by initial crack density or pore volume distribution
and cannot be compared directly; however, normalized crack growth fraction revealed an increase between 29 and 52 % for
FT-1 compared to an increase between 2 and 12 % for FT-2 (Fig. 6a, d). The increase varied between samples of different
545 saturation levels. While the low number of samples prohibit a quantitative analysis of saturation effects on rock damage, our
results are consistent and reveal higher damage of FT-1 compared to FT-2 independent of saturation levels (Fig. 6a, d).

Freeze-Thaw (FT-1) Cycles



Sustained Freezing (FT-2) Cycle



550 Figure 6: Freeze-thaw cycles (FT-1) have a higher frost cracking efficacy compared to a sustained freezing-cycles (FT-1) in low-porosity crack-dominated alpine rocks. Normalized crack fraction in relation to accumulated AE hits, simulated summed ice stress and thermal stress for a-c) FT-1 and d-f) FT-2. Simulated stresses by our frost cracking models are higher for FT-2 in comparison to FT-1 which is not aligned by normalized crack fraction.

555 The setup of FT-1 enables the development of thermal stresses during cooling and warming of the samples, volumetric expansion alongside the expanding freezing front and ice segregation during freezing conditions (Fig. 7a). In addition, FT-2 favours the development of ice segregation when temperatures are sustained, and rock moisture is able to migrate towards the freezing front (Fig. 7a).

560 During warming and cooling thermal stresses with a magnitude slightly higher than 1 MPa occurred. Due to the higher number of temperature cycles in FT-1, higher cumulative thermal stresses occurred in FT-1 than FT-2 (Fig. 6c,f), which could contribute to the increased rock damage observed and quantified via μ CT (Fig. 5g-l). Nonetheless, when compared to the predicted ice stresses (Fig. 6b,e) or accumulated AE hits during freezing times (Fig. 7), the thermal stresses were significantly lower, pointing to frost cracking as the predominant cause of rock damage.

565 Simulated stresses by our frost cracking models are higher for FT-2 in comparison to FT-1 (Fig. 6b,e) which is not supported by our μ CT findings (Fig. 5g-l). Our frost cracking modelling revealed eight times higher ice stresses in the sustained freezing phase than the freeze-thaw cycle. A fundamental requirement for our frost cracking model is complete saturation, a condition not consistently met throughout the experiment due to evaporation affecting our samples. The highly saturated samples showed in contrast to our model predictions, that highest frost damage (+53 % more crack volume than initially) occurred during FT-1, whilst in FT-2 significantly less crack growth (+5 % more crack volume than initially) was observed (Fig. 5i,l). This observation could potentially be explained by variations in ice formation. Gerber et al. (2023) suggests that the pressures exerted by ice depend on its structure, which in turn is influenced by the rate of ice formation and its aging process. Rapid freeze-thaw cycles may result in fine-grained ice and a sharp increase in stresses, whereas prolonged freezing, through aging, may result in coarse ice grains exerting less stress. Nevertheless, the transformation and aging of ice over an extended period of freezing – a characteristic of alpine conditions – could result in an increase in ice stress, thereby enhancing the potential for frost damage. A different explanation could be that ice segregation relies on water migration towards the freezing front, facilitated by the presence of unfrozen water at the top of our samples. Gerber et al. (2023)Our experiments have shown that we can visualize and quantify freeze thaw induced rock damage in low porosity rock samples, considering potential small additional damage that may be below μ CT resolution. Previous laboratory freeze thaw tests have used a decrease in elastic properties such as P wave velocity, Young's modulus or increases in porosity as a proxy for frost damage. However, in low porosity alpine rock frost damage is difficult to detect because changes in elastic properties or porosity are small or below the level of detection. Furthermore, the use of measured elastic properties or porosities does not provide information on crack geometry and crack growth. We demonstrated that cracks grow along pre-existing cracks and showed that that μ CT is a powerful analytical tool.

570
575
580

4.2 Potential thermal and ice stress sources inducing cracking

585 Thermal and ice stresses or a combination of these stresses can cause rock damage. We monitored AE as a proxy for cracking as previous stress experiments and analysed the timing of AE events in combination with simplified thermal stress and ice stress models to decipher the potential stress source.

590 Cooling of the samples induced thermal stresses (Fig. 4e-f) and triggered AE events (Fig. 4c-d) which we interpret as crack propagation similar to previous studies. When temperatures dropped below 0 °C, freezing enabled the development of ice stresses which could have amplified thermal-induced crack propagation. According to the volumetric expansion theory, ice stresses should develop in samples with a saturation higher than 91%. Moreover, indicate that various ice structures could affect water migration needed for ice segregation differently lowering its impact. Prick (1997) empirical findings suggested the existence of a saturation threshold between 58 and 100 % for the occurrence of volumetric expansion or ice segregation. However, measurements were conducted mostly on highly porous homogeneous limestone samples with porosities between 9.15 and 47.23 % which differ strongly to our low porous and crack dominated alpine rock. Only the Comblanchien limestone with a porosity of 1.3% was in the range of our samples porosity and showed a critical saturation threshold of 100 %. In addition, all rocks tested by had an intergranular porosity which differs to our fracture controlled alpine rock samples which impacts fracture propagation behaviour. We conclude that only our 100 % saturated samples fulfil the moisture conditions for volumetric expansion and consequently we cannot exclude the occurrence of volumetric expansion within these samples. 600 However, while temperatures dropped below the freezing point in our experiments, our AE data showed no significant differences in timing of AE signals between fully saturated samples and partially (70 %) or low saturated samples (30 %). Ice segregation simulations during cooling revealed a slight increase of ice stresses which were nevertheless still below the critical threshold (13.4 MPa) for crack propagation for our samples (Fig. 4e,f). In conclusion, we interpret the AE activity as a result of thermal stresses during cooling and before the freezing point which was eventually amplified by ice segregation induced stressed at temperatures below the freezing point (Fig. 4e-f). 605

During further cooling of the rock samples, ice segregation causes crack propagation and therefore pore space growth. The highest increase of AE hits was observed during freezing at temperatures significantly below the freezing point (below -6 °C in FT 1 and FT 2, see Fig. 7) which we interpret as acoustic emission events caused by frost cracking induced crack growth. 610 This temperature range is lower than the frost cracking window for Berea sandstone which lies between -3 and -6 °C observed by but consists with findings of on Wetterstein limestone (similar to Dachstein limestone) who suggested a maximum efficacy below -7 °C. The discrepancy can be explained by different pore geometries of grain supported Berea sandstone and fracture dominated Dachstein limestone and rock strength. The poor coupling of the bottom rock temperature sensor during the first five freeze thaw cycles of FT 1 resulted in underestimation of rock temperatures (between -2 and -4 °C) that reduced predicted ice pressure by our frost cracking model. In general, the AE pattern is consistent with simulated ice pressure due to ice 615

segregation that increase with decreasing freezing temperatures (Fig. 4e-f). Therefore, we suggest that unfrozen water migrated towards the freezing front as previously observed in laboratory studies and caused crystallization pressures inducing cracking. The highest increase of AE hits we observed in the partially saturated (70 %) rock samples in FT 1 and FT 2 resulting in the highest number of AE events. In contrast, the low-saturated (30 %) samples showed the lowest number of AE hits in FT 1 and FT 2 which differs to findings of [1] who suggested no lower moisture boundary for ice segregation under the prerequisite of available water within short distance (0.4 m). However, our setup did not contain an external water bath like [1] which may not provide sufficient water for ice segregation in our low-saturated (30 %) samples. Based on AE activity our experiments suggest that higher saturation increases ice segregation. As our ice stress modelling assumes full saturation, we cannot test the effect of different saturation regimes on model behaviour.

Compared to cooling, the warming stage caused less cracking indicated by AE events in FT 1 (Fig. 7a-e) as thermal stresses increased but ice stresses were reduced due to thawing. Previous laboratory measurements by [2] revealed a maximum thermal stress during warming, however, the authors used much higher temperature ranges (up to 1000 °C). In alpine rockwalls, [3] observed more crack opening during cooling compared to warming and interpreted this pattern as a result of thermal stresses in combination with ice stresses. Our stress modelling (Fig. 4e) shows peak thermal stress with increasing ice stresses that support this argument and suggest a combination of thermal and ice segregation induced stress resulted in higher as expected AE hits during cooling cycles.

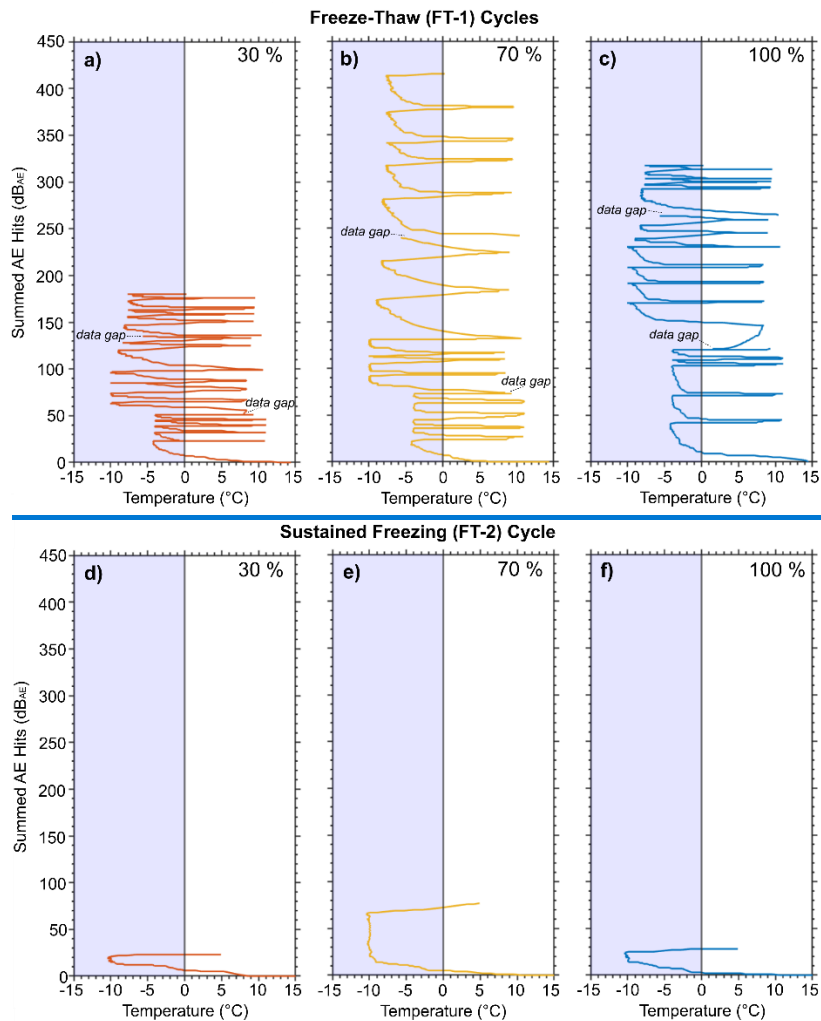


Fig. 7: Cumulative AE hits in relation to bottom rock temperature for a) FT-1 and d) FT-2.

635 4.3 Efficacy of freeze-thaw and sustained-freezing cycles

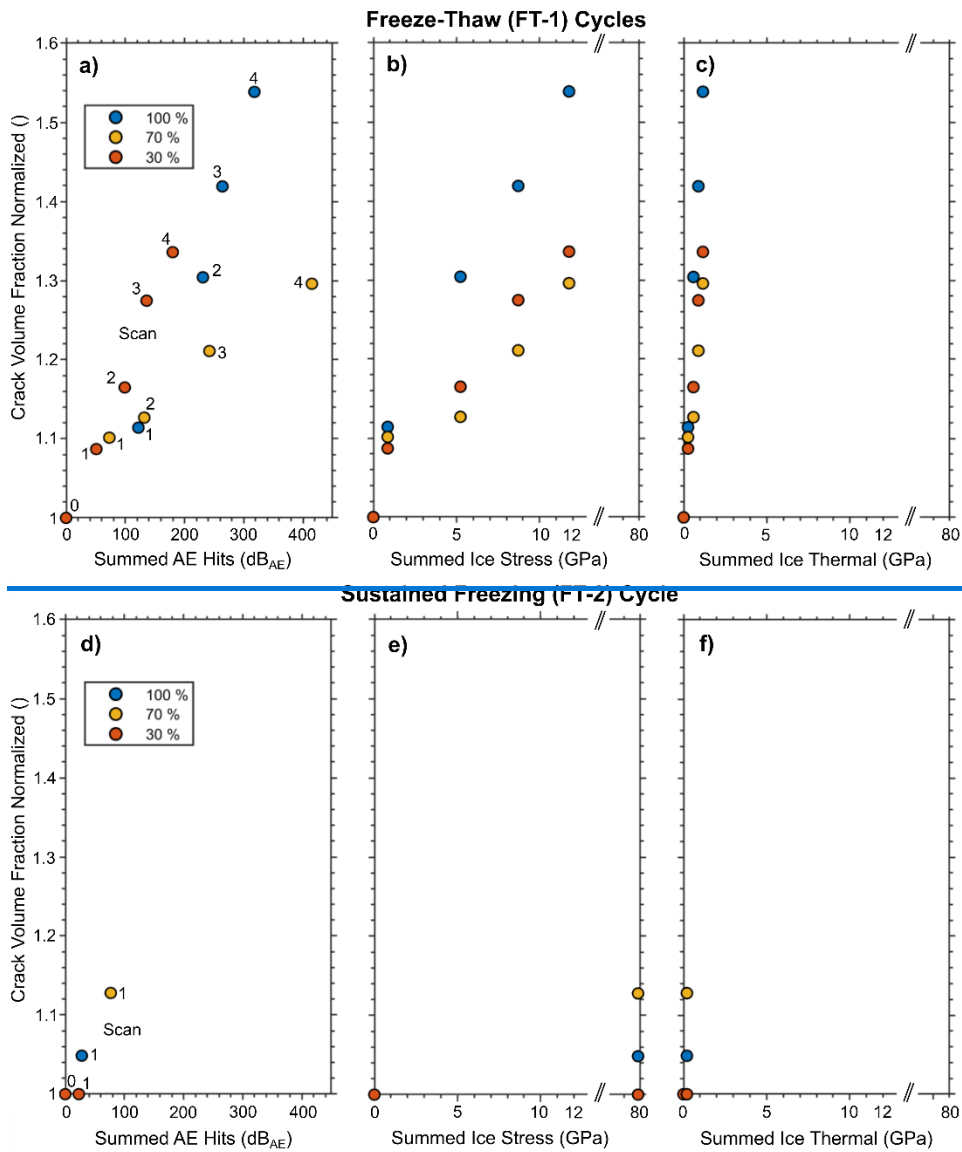
Freeze-thaw cycles (FT-1) have a higher frost cracking efficacy compared to a sustained-freezing cycles (FT-2) in low-porosity crack-dominated alpine rocks. Absolute crack growth is affected by initial crack density or volume and cannot be compared directly; however, normalized crack growth fraction revealed an increase between 34 and 52% (FT-1) compared to an increase between 2 and 12% (FT-2) (Fig. 8a, d). Based on μ CT data, saturation levels have a minor impact on rock damage patterns, yet highest fracturing during FT-1 was observed in the fully saturated sample followed by the 30% saturated sample in contrast to patterns observed by AE data (Fig. 8a). FT-2 revealed higher cracking in the 70% saturated sample followed by the full saturation sample which is in accordance with AE data (Fig. 8d). We used AE data to determine the source of cracking by analysing the timing of AE hits. AE was used frequently as a proxy for thermal stress cracking in the field, frost cracking in

640

the laboratory or field measurements. Our results show that the number of AE events and quantified rock damage by μ CT are proportional (Fig. 8a,d), however, highest overall number of AE hits are not always in accordance with highest visible rock damage (Fig. 8a). The 70 % saturated sample revealed more than 415 AE hits with a normalized crack growth fraction of 47 %, while the 30 % saturated sample showed 180 AE hits and 53 % crack growth. This pattern could result from different volume growth per crack propagation forcing less AE releases with higher crack growth. However, our natural rock samples may react in a different manner to stresses due to their slightly varying rock parameters which could affect number of AE hits.

Predicted stresses by our models are higher for FT-2 in comparison to FT-1 which is not supported by our μ CT findings. Our frost cracking modelling revealed eight times higher ice stresses in the sustained freezing phase than the freeze-thaw cycle (Fig. 8b,e). A prerequisite for our frost cracking model is a full saturation which applies for the 100 % saturated samples in FT-1 and -2. Fully saturated samples showed in contrast to our model predictions, that highest frost damage (+53 % more crack volume than initially) occurred during FT-1, whilst in FT-2 significantly less crack growth (+5 % more crack volume than initially) was observed. A reason for this pattern could be the occurrence of volumetric expansion that our frost cracking model does not incorporate. In addition, ice segregation requires water migration towards the freezing front that we provided by unfrozen water in the top of our samples. Observed water migration in limestone samples of comparable size with porosities between 26 and 48.2 %. However, our sampled rocks have porosities of 0.1% which provide only a limited water reservoir potentially. Consequently, the water reservoir in FT-2 was the limiting factor for ice segregation despite temperature ranges favoring ice segregation.

Observed water migration in limestone samples similar in size, with porosities ranging from 26 to 48.2 %. In contrast, our rock samples exhibit much lower porosities of around 0.1%, offering a substantially smaller water reservoir. This suggests that the water supply in FT-2 may have been also a limiting factor for ice segregation, despite the temperature conditions being conducive to this process (e.g. Walder and Hallet, 1985) and therefore, As a result, our ice stress simulations eventually of ice stress might have overestimated the actual stresses involved. In addition, our frost cracking model simplified the complex crack geometries observed in the samples (Fig. 5) and simulated a single 1 mm long crack. Therefore, the magnitude of modelled/simulated ice stresses potentially deviates significantly from occurred ice stresses which resulted in the deviation between modelled ice stresses and measured rock damage especially in FT-2 (Fig. 8b,e).



670 **Figure 8: Normalized crack volume fraction in relation to accumulated AE hits, simulated summed ice stress and thermal stress for a-c) FT-1 and d-f) FT-2.**

675 During freezing of water to ice, volume expansion occurs that can produce rock damage if saturation levels are above 91%. The high number of freezing cycles in FT-1 could result in more volume expansion induced frost cracking as in FT-2. The full saturated sample in FT-1 revealed the highest normalized rock damage (53 %) compared to partially (29% increase) and low (34% increase) saturated samples (Fig. 5g,h), which could indicate the involvement of volumetric expansion. We only estimated initial saturation and rock moisture can redistribute during the experiments resulting in higher moisture levels at the

680

freezing fronts that could exceed moisture threshold enabling volume expansion induced damage. In addition to volume expansion, higher saturation can also increase the efficacy of ice segregation by providing more moisture able to migrate. We conclude that within the constraints of our experiments freeze-thaw cycles cause higher frost damage compared to sustained freezing cycles with ice segregation serving as the primary contributing factor to frost cracking while the occurrence of volume expansion induced damage is likely within high saturated samples and cannot be exclude in low and partially saturated samples.

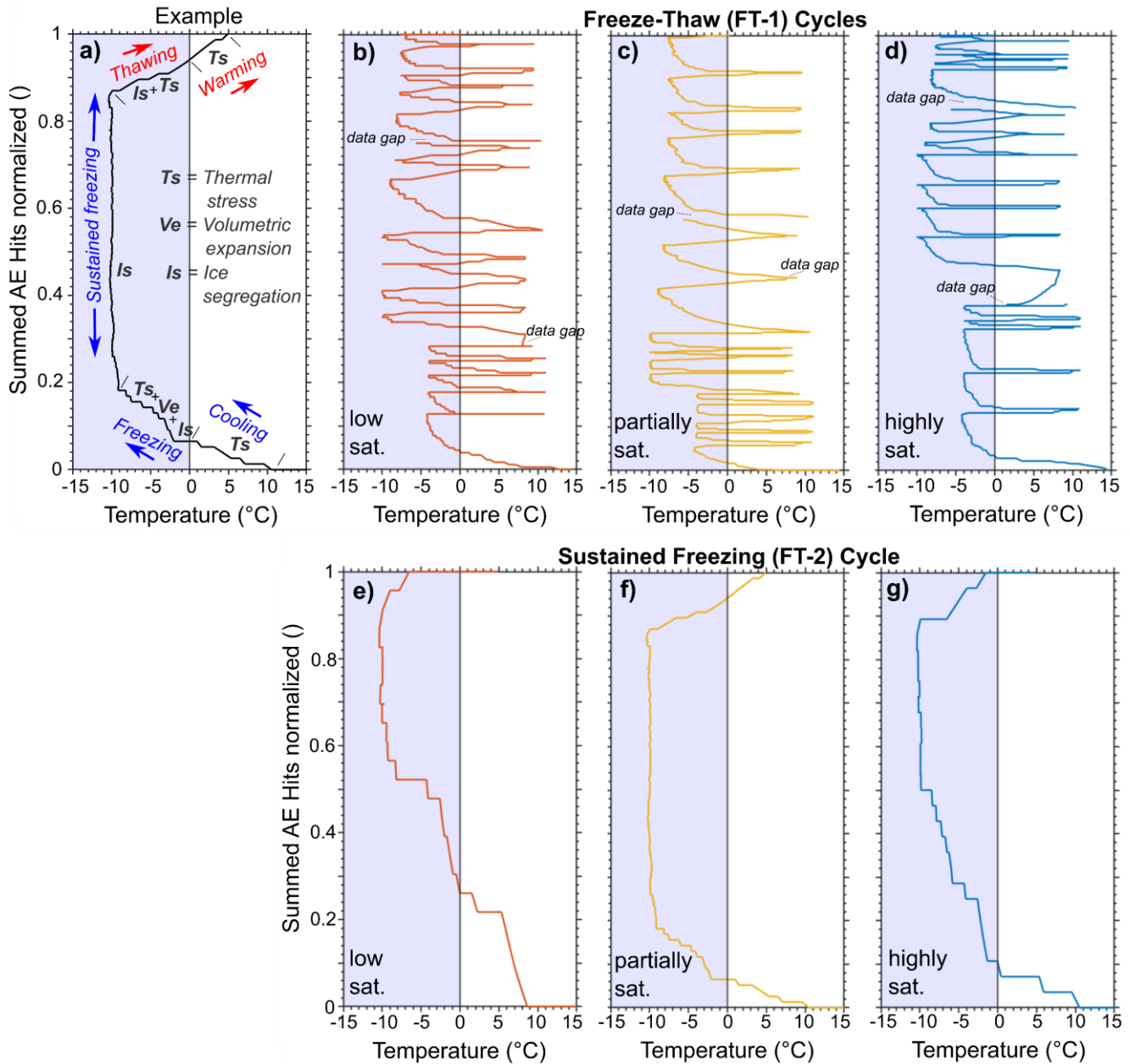


Figure 7: Cooling phases accumulate more AE hits compared to warming phases, suggesting frost cracking as the main contributor to rock damage. a) Timing examples of potential stress occurrences include thermal stresses during sample cooling and warming, volumetric expansion along with the expanding freezing front, and ice segregation under freezing conditions. Cumulative AE hits are plotted against the bottom rock temperature sensor for b-d) FT-1 and e-g) FT-2.

4.4 Implications for ~~rock weathering in~~ alpine rockwalls

695 Our results revealed that the presence and arrangement of voids and fractures within rock significantly impact frost damage. We have shown that micro-crack expansion tends to follow pre-existing fractures, extending their width and length (Fig. 4 and 5g-l), leading to a gradual increase in crack size. As a result, samples with a higher crack density experience more severe frost damage. In natural rockwalls, both micro and macro cracks are present, the latter often arising from tectonic forces and/or weathering effects. These fractures play a crucial role for erosion processes as they influence rock cohesion and modify the dynamics, patterns, and locations of geomorphic activities on various spatial and temporal scales. (Scott and Wohl, 2019).

700 Studies by Hales and Roering (2009) and Draebing and Mayer (2021) have established a link between frost cracking intensity and the density of fractures, with rockwalls exhibiting more fractures also showing greater evidence of frost cracking. Furthermore, Eppes et al. (2018) have demonstrated through both field and laboratory observations that an increase in the length and quantity of cracks leads to higher long-term erosion rates. Neely et al. (2019) revealed that higher fracture density decreases steepness of cliffs and increases catchment erosion rates. In New Zealand, Clarke and Burbank (2010) showed that

705 bedrock fracturing by geomorphic processes including weathering controls the depths of erosive processes as bedrock landsliding. We infer that upscaling our findings from micro to macro cracks highlights the connection between erosion and fracture density. However, such extrapolation must consider the scale dependencies and complex fracture interactions influenced by broader geological and environmental factors, including tectonic forces, weathering effects, and variations in material properties, which could significantly modify erosion dynamics beyond micro-scale observations.

710 Our findings indicate that frost cracking is more effective during freeze-thaw cycles than during prolonged periods of freezing. Matsuoka et al. (1998) indicated that south-facing rockwalls typically undergo more freeze-thaw cycles due to lack of snow cover, whereas those facing north are subject to longer durations of freezing. This leads to the initial assumption that south facing rockwalls would sustain more frost damage, contributing to increased erosion. However, few existing empirical data indicates that erosion rates are actually 2.5 to 3 times (Sass, 2005b) or up to one magnitude (Coutard and Francou, 1989) higher

715 on north-facing rockwalls. Matsuoka et al. (1998) suggested that while freeze-thaw cycles can cause shallow frost damage (up to 0.3 m deep), prolonged freezing can result in more significant frost damage (up to 5 m deep), leading to larger rockfalls. This indicates that the temporal scale of freeze-thaw cycles plays a crucial role in determining weathering and erosion rates, a concept further supported by Matsuoka (2008), who found that short-term freeze-thaw cycles cause minor crack expansion, whereas long-term freezing leads to more substantial crack widening.

720 Our research suggests a direct correlation between the frequency of AE events and the extent of rock damage, as measured by μ CT scanning. However, the highest occurrences of AE hits do not consistently correspond to the most significant observable rock damage. This discrepancy could be attributed to ice formation influenced by thermal gradients, as well as changes and aging in the ice, as discussed by Gerber et al. (2023). This insight has implications for studies that employ AE as an indicator for thermal stress-induced cracking (Eppes et al., 2016; Collins et al., 2018) and frost cracking (Amitrano et al., 2012; Girard

725 et al., 2013) in natural rockwalls.

The estimated ice stresses in our simulations may significantly diverge from the actual ice stresses experienced, leading to differences between simulated ice stresses and observed rock damage, particularly in the FT-2 scenario. This mismatch between model predictions and actual frost damage observations could stem from the model's oversimplified representations of crack geometries and rock properties, or the relatively brief duration of sustained freezing in FT-2 when compared to conditions on a real rockwall. Research efforts such as those by Draebing and Mayer (2021) or Sanders et al. (2012) which utilize frost cracking models to assess frost damage, might have overemphasized the effects of frost weathering. Nonetheless, Draebing et al. (2022) The number of freeze thaw cycles or sustained freezing periods within north facing rockwalls is controlled by its elevation and snow cover (Fig. 2a). At elevations above 3000 m, as at Corvatsch, Matterhorn and Aiguille di Midi (Fig. 2a-b) sustained freezing periods are dominant throughout the year with likely permafrost occurrence. At elevations around 3000 m such as Dachstein or Gemsstock, the magnitude of freezing is decreased and the length of the sustained freezing period is controlled by snow cover. These rockwalls are at the fringe of permafrost and show permafrost conditions in shaded rockwall areas. Snow duration decreases with elevation and at lower elevation, such as Dammkar, sustained freezing is of short duration and the number of freeze thaw cycles increase as temperatures fluctuate between positive and negative rock temperatures especially in autumn and spring (Fig. 2b). A higher efficacy of freeze thaw cycles than sustained freezing would result in higher erosion rates at low elevation rockwalls, however, a requirement for reasonable frost damage are sufficiently cold temperatures to promote crack growth in high strength rock which is to some extent fulfilled at low elevated sites. In addition, reviewed rockwall erosion rates in the European Alps and showed an elevation dependent increase of erosion. The authors suggest that the erosion rates increase as a result of frost cracking, permafrost and paraglacial processes. South facing rockwalls in the Alps experience more freeze thaw cycles and less sustained freezing due to higher average rock temperatures and shorter snow duration. Previous studies observed an increase of mean annual rock surface temperatures in south facing rockwalls compared to north facing rockwalls between 2.2 to 6°C in the Hungerli Valley, between 3.3°C and 3.8°C at Gemsstock, up to 3.9°C at the Steintaelli, up to 5°C at Aiguille du Midi and up to 7°C at Matterhorn and Jungfraujoeh. Snow duration significantly decreases in south facing rockwalls which results in an increase of freeze thaw cycles. A higher efficacy of frequent freeze thaw cycles would result in more frost cracking at south facing rock walls and higher erosion rates compared to north facing rockwalls. Frost cracking modelling revealed more frost damage on south facing rockwalls in the Hungerli that authors attribute to high changes of thermal gradients. The authors suggested that the frost cracking magnitudes are overestimated due to assumed unrealistic moisture conditions and demonstrated that frost cracking patterns deviate from measured fracture systems. Erosion rate measurements revealed higher erosion rates at north facing rockwalls than south facing rockwalls in the Alps. Differences between efficacy of freeze thaw cycles and erosion rates can relate to process involved in erosion that are not included in frost cracking models such as permafrost or paraglacial processes that need to be taken into account.

Climate change can accelerate or impede frost weathering efficacy in the Alps. Global warming influences temperature elevational patterns in the mountains leading to warming, reduced snow season and stronger temperature fluctuations. Our results show that the efficacy of frost weathering is dependent on number of freeze thaw cycles and sustained freezing periods

760 regarding sufficient temperatures for frost cracking. Warming at elevations above 3000 m will lead to warmer mean annual
rock surface temperatures and a reduced snow duration that will amplify the occurrence of frequent freeze-thaw cycles and
decrease sustained freezing and result in temperature conditions as currently observed at south-facing rockwalls. At low-
elevated rockwalls such as the Dammkar (Fig. 1a), warming will decrease the number of freeze-thaw cycles and, therefore,
765 efficacy of frost cracking. The shift of frost weathering will provide more erosion at high-elevation sites and effect debris flow
activity due to changes of sediment availability and therefore changes hazard potential at the valley bottom.
showed that frost weathering simulations do correspond with the erosion rates observed on north-facing rockwalls, where
extended periods of freezing are more common.

5 Conclusion

770 ~~We quantified~~ In our investigation of frost-induced rock damage on Dachstein limestone ~~by combining, we employed~~ X-ray
computed micro-tomography (μ CT), acoustic emission (AE) monitoring, and frost cracking modelling. ~~To differentiate to~~
assess the damage. We aimed to distinguish between ~~potential different~~ mechanisms of rock damage, ~~by simulating~~ thermal-
and ice-induced stresses ~~were simulated and compared correlating them~~ with AE activity, ~~in samples with varying saturation~~
levels. Our ~~study showed~~ research demonstrated that μ CT ~~can be used to quantify effectively~~ measures frost damage in low-
775 porosity (0.1%) rock. ~~Overall, rock, primarily revealing~~ damage ~~occurred by propagation through the expansion or deepening~~
of ~~pre-existing~~ cracks rather than ~~by initiation of new cracks~~. ~~AE activity, thermal and ice stress model~~ the creation of new
ones. Our findings also revealed that the presence and distribution of voids and cracks significantly influence frost damage,
with rocks having a higher initial crack density exhibiting more damage. A direct link was found between the rate of AE events
780 and the degree of rock damage as determined by μ CT, however, the most frequent AE hits did not always match the areas of
greatest visible damage, suggesting complexities in the relationship between AE activity and rock damage.
Our studies suggest that rock damage is ~~predominantly caused by~~ primarily a ~~combination result~~ of thermal stresses and frost
cracking during cooling phases, with frost cracking identified as a key contributor to damage. Yet, the ice stresses predicted
by our simulations might greatly differ from the actual stresses, potentially due to the model's simplified assumptions or the
short duration of sustained freezing in our FT-2 scenario. Analysis of μ CT data revealed that repeated freeze-thaw cycles (FT-
785 1) resulted in more effective cracking compared to extended periods of freezing (FT-2). This observation contrasts with field
study outcomes that associate frost damage and rockwall erosion, showing greater erosion rates on north-facing rockwalls,
which typically undergo longer periods of sustained freezing rather than freeze-thaw cycles. We assume that the limited water
accessibility in FT-2, due to the samples' low porosity or the dynamics of ice segregation during cooling. ~~In the formation, and~~
the short experiment time might explain this discrepancy. Given the finite sample size and varied saturation levels, our
790 experiments suggest that higher levels of saturation tend to increase frost-induced rock damage, as inferred from acoustic
emission activity. This preliminary evidence emphasizes the need for additional research to fully saturated samples, the
occurrence of volumetric expansion cannot be excluded as a potential amplifier of damage. At temperatures below -6°C , AE
data in combination with understand saturation's impact on frost damage.

795

Data availability

800 Data is available at UU depository.

~~Code for frost cracking modelling indicate rock damage driven by ice segregation, while during warming thermal stress modelling suggests further rock damage by thermal stress. In summary, ice stresses were the dominant factor of rock damage, however, magnitude of AE activity and frost cracking model results for different saturation regimes differ from rock damage quantified by μ CT, which we interpret as a result of complex crack geometry, saturation assumptions of frost cracking models and unknown triggers of AE activity. Based on μ CT results, frequent freeze thaw cycles (FT 1) showed higher cracking efficiencies than sustained freeze thaw cycles (FT 2). This pattern could be a result of limited water availability in FT 2 due to the low porosity of our samples. For natural rockwalls, our results indicate higher frost cracking activity in low elevation or south facing rockwalls where frequent freeze thaw cycles are currently more common. However, our results contradict the few available erosion measurements. Further testing of the limiting factor of water availability should be undertaken as modelled ice stresses differ from quantified rock damage in FT 2.~~ is available at: https://github.com/TillM90/Code_frost_cracking_model.git

810

Data availability

~~Data will be uploaded to a data depository when the paper is accepted. Until then, data is available on request from the corresponding author.~~

815

Author Contribution

TM, MD, LS and DD designed the experiments. TM, MD and LS conducted the experiments and TM processed the data with support by MD and LS. ~~TM, MD, LS, VC~~ and DD ~~contributed to~~ wrote the manuscript with contributions from MD, LS and editing VC.

820

Conflict of Interest Statement

The authors declare that they have no conflict of interest.

Acknowledgements

825 This project has received funding from the European Union's Horizon 2020 research and innovation programme under grant agreement No 101005611 for Transnational Access conducted at Ghent University. The laboratory work was funded by

EXCITE grants FROST (EXCITE_TNA_C1_2022_06) and CRACK (EXCITE_TNA_C2_2022_004), and by German Research Foundation (DR1070/3-1, 426793773). [The authors We acknowledge the valuable comments by Norikazu Matsuoka and one anonymous reviewer that improved this manuscript. We](#) thank Timo Sprenger for his help at collecting rock samples in the field [and the Dachstein cable car team for logistic support](#). The Ghent University Special Research Fund (BOF-UGent) is acknowledged to support the Centre of Expertise UGCT (BOF.COR.2022.0009).

References

- 1097-6:2022-5, D.-E.: Tests for mechanical and physical properties of aggregates - Part 6: Determination of particle density and water absorption; German version EN 1097-6:2022, 64 pp., <https://dx.doi.org/10.31030/3290441>.
- 52102:2006-02, D.-E.: Test methods for aggregates - Determination of dry bulk density by the cylinder method and calculation of the ratio of density, 9 pp.
- Amitrano, D., Gruber, S., and Girard, L.: Evidence of frost-cracking inferred from acoustic emissions in a high-alpine rock-wall, *Earth and Planetary Science Letters*, 341-344, 86-93, <https://dx.doi.org/10.1016/j.epsl.2012.06.014>, 2012.
- Anderson, R. S.: Near-surface thermal profiles in alpine bedrock: Implications for the frost weathering of rock, *Arct. Alp. Res.*, 30, 362-372, <https://dx.doi.org/10.2307/1552008>, 1998.
- Bazant, Z. P. and Planas, J.: *Fracture and Size Effect in Concrete and Other Quasibrittle Materials 1st*, New York, <https://dx.doi.org/10.1201/9780203756799> 1998.
- Carloni, C., Santandrea, M., and Baietti, G.: Influence of the width of the specimen on the fracture response of concrete notched beams, *Engineering Fracture Mechanics*, 216, 106465, <https://dx.doi.org/10.1016/j.engfracmech.2019.04.039>, 2019.
- Cermák, V. and Rybach, L.: Thermal conductivity and specific heat of minerals and rocks, in: *Landolt-Börnstein Zahlenwerte und Funktionen aus Naturwissenschaften und Technik, Neue Serie, Physikalische Eigenschaften der Gesteine (V/1a)*, edited by: Angenheister, G., Springer, Berlin, 305–343, 1982.
- Clarke, B. A. and Burbank, D. W.: Bedrock fracturing, threshold hillslopes, and limits to the magnitude of bedrock landslides, *Earth and Planetary Science Letters*, 297, 577-586, <https://doi.org/10.1016/j.epsl.2010.07.011>, 2010.
- Cnudde, V. and Boone, M.: High-resolution X-ray computed tomography in geosciences: a review of the current technology and applications, *EARTH-SCIENCE REVIEWS*, 123, 1-17, [10.1016/j.earscirev.2013.04.003](https://doi.org/10.1016/j.earscirev.2013.04.003), 2013.
- Collins, B. D., Stock, G. M., Eppes, M.-C., Lewis, S. W., Corbett, S. C., and Smith, J. B.: Thermal influences on spontaneous rock dome exfoliation, *Nature Communications*, 9, 762, <https://dx.doi.org/10.1038/s41467-017-02728-1>, 2018.
- Coutard, J.-P. and Francou, B.: Rock Temperature Measurements in Two Alpine Environments: Implications for Frost Shattering, *Arct. Alp. Res.*, 21, 399-416, <https://dx.doi.org/10.2307/1551649>, 1989.
- De Kock, T., Boone, M. A., De Schryver, T., Van Stappen, J., Derluyn, H., Masschaele, B., De Schutter, G., and Cnudde, V.: A Pore-Scale Study of Fracture Dynamics in Rock Using X-ray Micro-CT Under Ambient Freeze–Thaw Cycling, *Environmental Science & Technology*, 49, 2867-2874, <https://dx.doi.org/10.1021/es505738d>, 2015.
- Deprez, M., De Kock, T., De Schutter, G., and Cnudde, V.: The role of ink-bottle pores in freeze-thaw damage of oolitic limestone, *Construction and Building Materials*, 246, 118515, <https://dx.doi.org/10.1016/j.conbuildmat.2020.118515>, 2020a.
- Deprez, M., De Kock, T., De Schutter, G., and Cnudde, V.: A review on freeze-thaw action and weathering of rocks, *Earth-Science Reviews*, 203, 103143, <https://dx.doi.org/10.1016/j.earscirev.2020.103143>, 2020b.
- Derjaguin, B. V. and Churaev, N. V.: Flow of nonfreezing water interlayers and frost heaving, *Cold Regions Science and Technology*, 12, 57-66, [https://dx.doi.org/10.1016/0165-232X\(86\)90020-0](https://dx.doi.org/10.1016/0165-232X(86)90020-0), 1986.
- Dewanckele, J., Boone, M. A., De Kock, T., De Boever, W., Brabant, L., Boone, M. N., Fronteau, G., Dils, J., Van Hoorebeke, L., Jacobs, P., and Cnudde, V.: Holistic approach of pre-existing flaws on the decay of two limestones, *Science of The Total Environment*, 447, 403-414, <https://doi.org/10.1016/j.scitotenv.2012.12.094>, 2013.
- Draebing, D.: Identification of rock and fracture kinematics in high Alpine rockwalls under the influence of elevation, *Earth Surface Dynamics*, 9, 977-994, <https://dx.doi.org/10.5194/esurf-9-977-2021>, 2021.
- Draebing, D. and Krautblatter, M.: P-wave velocity changes in freezing hard low-porosity rocks: a laboratory-based time-average model, *The Cryosphere*, 6, 1163-1174, <https://dx.doi.org/10.5194/tc-6-1163-2012>, 2012.
- Draebing, D. and Krautblatter, M.: The Efficacy of Frost Weathering Processes in Alpine Rockwalls, *Geophysical Research Letters*, 46, 6516-6524, <https://dx.doi.org/10.1029/2019gl081981>, 2019.
- Draebing, D. and Mayer, T.: Topographic and geologic controls on frost cracking in Alpine rockwalls, *Journal of Geophysical Research: Earth Surface*, 126, e2021JF006163, <https://dx.doi.org/10.1029/2021JF006163>, 2021.

- Draebing, D., Krautblatter, M., and Hoffmann, T.: Thermo-cryogenic controls of fracture kinematics in permafrost rockwalls, *Geophysical Research Letters*, 44, 3535-3544, <https://dx.doi.org/10.1002/2016GL072050>, 2017a.
- Draebing, D., Mayer, T., Jacobs, B., and McColl, S. T.: Alpine rockwall erosion patterns follow elevation-dependent climate trajectories, *Communications Earth & Environment*, 3, 21, <https://dx.doi.org/10.1038/s43247-022-00348-2>, 2022.
- 880 Draebing, D., Haberkorn, A., Krautblatter, M., Kenner, R., and Phillips, M.: Thermal and Mechanical Responses Resulting From Spatial and Temporal Snow Cover Variability in Permafrost Rock Slopes, *Steintaeli, Swiss Alps, Permafrost and Periglacial Processes*, 28, 140-157, <https://dx.doi.org/10.1002/ppp.1921>, 2017b.
- Duca, S., Occhiena, C., Mattone, M., Sambuelli, L., and Scavia, C.: Feasibility of Ice Segregation Location by Acoustic Emission Detection: A Laboratory Test in Gneiss, *Permafrost And Periglacial Processes*, 25, 208-219, 10.1002/ppp.1814, 2014.
- 885 Egholm, D. L., Andersen, J. L., Knudsen, M. F., Jansen, J. D., and Nielsen, S. B.: The periglacial engine of mountain erosion - Part 2: Modelling large-scale landscape evolution, *Earth Surface Dynamics*, 3, 463-482, <https://dx.doi.org/10.5194/esurf-3-463-2015>, 2015.
- Eppes, M.-C. and Keanini, R.: Mechanical weathering and rock erosion by climate-dependent subcritical cracking, *Reviews of Geophysics*, 55, 470-508, <https://dx.doi.org/10.1002/2017RG000557>, 2017.
- Eppes, M. C., Magi, B., Hallet, B., Delmelle, E., Mackenzie-Helnwein, P., Warren, K., and Swami, S.: Deciphering the role of solar-induced thermal stresses in rock weathering, *Geological Society of America Bulletin*, 128, 1315-1338, <https://dx.doi.org/10.1130/b31422.1>, 2016.
- Eppes, M. C., Hancock, G. S., Chen, X., Arey, J., Dewers, T., Huettnermoser, J., Kiessling, S., Moser, F., Tannu, N., Weiserbs, B., and Whitten, J.: Rates of subcritical cracking and long-term rock erosion, *Geology*, 46, 951-954, 10.1130/G45256.1, 2018.
- Eslami, J., Walbert, C., Beaucour, A.-L., Bourges, A., and Noumowe, A.: Influence of physical and mechanical properties on the durability of limestone subjected to freeze-thaw cycles, *Construction and Building Materials*, 162, 420-429, <https://dx.doi.org/10.1016/j.conbuildmat.2017.12.031>, 2018.
- 895 Everett, D. H.: The thermodynamics of frost damage to porous solids, *Transactions of the Faraday Society*, 57, 1541-1551, <https://dx.doi.org/10.1039/TF9615701541>, 1961.
- Gerber, D., Wilen, L. A., Dufresne, E. R., and Style, R. W.: Polycrystallinity Enhances Stress Buildup around Ice, *Physical Review Letters*, 131, 208201, 10.1103/PhysRevLett.131.208201, 2023.
- 900 Gerber, D., Wilen, L. A., Poydenot, F., Dufresne, E. R., and Style, R. W.: Stress accumulation by confined ice in a temperature gradient, *Proc Natl Acad Sci U S A*, 119, e2200748119, <https://dx.doi.org/10.1073/pnas.2200748119>, 2022.
- Gilpin, R. R.: A model of the "liquid-like" layer between ice and a substrate with applications to wire regelation and particle migration, *Journal of Colloid and Interface Science*, 68, 235-251, [https://dx.doi.org/10.1016/0021-9797\(79\)90277-7](https://dx.doi.org/10.1016/0021-9797(79)90277-7), 1979.
- Gilpin, R. R.: A model for the prediction of ice lensing and frost heave in soils, *Water Resources Research*, 16, 918-930, <https://dx.doi.org/10.1029/WR016i005p00918>, 1980.
- 905 Girard, L., Gruber, S., Weber, S., and Beutel, J.: Environmental controls of frost cracking revealed through in situ acoustic emission measurements in steep bedrock, *Geophysical Research Letters*, 40, 1748-1753, <https://dx.doi.org/10.1002/grl.50384>, 2013.
- Hales, T. C. and Roering, J. J.: A frost "buzzsaw" mechanism for erosion of the eastern Southern Alps, New Zealand, *Geomorphology*, 107, 241-253, <https://dx.doi.org/10.1016/j.geomorph.2008.12.012>, 2009.
- 910 Hallet, B., Walder, J. S., and Stubbs, C. W.: Weathering by segregation ice growth in microcracks at sustained subzero temperatures: Verification from an experimental study using acoustic emissions, *Permafrost And Periglacial Processes*, 2, 283-300, <https://dx.doi.org/10.1002/ppp.3430020404>, 1991.
- Jia, H., Xiang, W., and Krautblatter, M.: Quantifying Rock Fatigue and Decreasing Compressive and Tensile Strength after Repeated Freeze-Thaw Cycles, *Permafrost and Periglacial Processes*, 26, 368-377, <https://dx.doi.org/10.1002/ppp.1857>, 2015.
- 915 Kjelstrup, S., Ghoreishian Amiri, S. A., Loranger, B., Gao, H., and Grimstad, G.: Transport coefficients and pressure conditions for growth of ice lens in frozen soil, *Acta Geotechnica*, 16, <https://dx.doi.org/10.1007/s11440-021-01158-0>, 2021.
- Lepique, M.: Empfehlung Nr. 10 des Arbeitskreises 3.3 "Versuchstechnik Fels" der Deutschen Gesellschaft für Geotechnik e. V.: Indirekter Zugversuch an Gesteinsproben – Spaltzugversuch, *Bautechnik*, 85, 623-627, <https://dx.doi.org/10.1002/bate.200810048>, 2008.
- Maji, V. and Murton, J. B.: Micro-computed tomography imaging and probabilistic modelling of rock fracture by freeze-thaw, *Earth Surface Processes and Landforms*, 45, 666-680, <https://doi.org/10.1002/esp.4764>, 2020.
- 920 Maji, V. and Murton, J. B.: Experimental Observations and Statistical Modeling of Crack Propagation Dynamics in Limestone by Acoustic Emission Analysis During Freezing and Thawing, *Journal of Geophysical Research: Earth Surface*, 126, e2021JF006127, <https://dx.doi.org/10.1029/2021JF006127>, 2021.
- Matsuoka, N.: Mechanisms of rock breakdown by frost action: An experimental approach, *Cold Regions Science and Technology*, 17, 253-270, [https://dx.doi.org/10.1016/S0165-232X\(05\)80005-9](https://dx.doi.org/10.1016/S0165-232X(05)80005-9), 1990.
- 925 Matsuoka, N.: Microgelivation versus macrogelivation: towards bridging the gap between laboratory and field frost weathering, *Permafrost and Periglacial Processes*, 12, 299-313, <https://dx.doi.org/10.1002/ppp.393>, 2001.
- Matsuoka, N.: Frost weathering and rockwall erosion in the southeastern Swiss Alps: Long-term (1994-2006) observations, *Geomorphology*, 99, 353-368, 10.1016/j.geomorph.2007.11.013, 2008.
- 930 Matsuoka, N.: A multi-method monitoring of timing, magnitude and origin of rockfall activity in the Japanese Alps, *Geomorphology*, 336, 65-76, <https://dx.doi.org/10.1016/j.geomorph.2019.03.023>, 2019.

- Matsuoka, N. and Murton, J.: Frost weathering: Recent advances and future directions, *Permafrost And Periglacial Processes*, 19, 195-210, <https://dx.doi.org/10.1002/ppp.620>, 2008.
- 935 Matsuoka, N., Hirakawa, K., Watanabe, T., Haeberli, W., and Keller, F.: THE ROLE OF DIURNAL, ANNUAL AND MILLENNIAL FREEZE-THAW CYCLES IN CONTROLLING ALPINE SLOPE INSTABILITY, Mayer, T., Eppes, M., and Draebing, D.: Influences Driving and Limiting the Efficacy of Ice Segregation in Alpine Rocks, *Geophysical Research Letters*, 50, e2023GL102951, <https://dx.doi.org/10.1029/2023GL102951>, 2023.
- Messenzehl, K., Viles, H., Otto, J.-C., Ewald, A., and Dikau, R.: Linking rock weathering, rockwall instability and rockfall supply on talus slopes in glaciated hanging valleys (Swiss Alps), *Permafrost and Periglacial Processes*, 29, 135-151, 10.1002/ppp.1976, 2018.
- 940 Murton, J. B., Peterson, R., and Ozouf, J.-C.: Bedrock Fracture by Ice Segregation in Cold Regions, *Science*, 314, 1127-1129, <https://dx.doi.org/10.1126/science.1132127>, 2006.
- Neely, A. B., DiBiase, R. A., Corbett, L. B., Bierman, P. R., and Caffee, M. W.: Bedrock fracture density controls on hillslope erodibility in steep, rocky landscapes with patchy soil cover, southern California, USA, *Earth and Planetary Science Letters*, 522, 186-197, <https://doi.org/10.1016/j.epsl.2019.06.011>, 2019.
- 945 Paul, G. C. D.: *Materials science & engineering*, CRC Press, Materials Park, Ohio:ASM International1991.
- Perras, M. A. and Diederichs, M. S.: A Review of the Tensile Strength of Rock: Concepts and Testing, *Geotechnical and Geological Engineering*, 32, 525-546, <https://dx.doi.org/10.1007/s10706-014-9732-0>, 2014.
- Pfiffner, O. A.: *Geologie der Alpen*, Haupt 359 pp., 10.36198/9783838584164, 2010.
- Prick, A.: Critical Degree of Saturation as a Threshold Moisture Level in Frost Weathering of Limestones, *Permafrost and Periglacial Processes*, 8, 91-99, [https://dx.doi.org/10.1002/\(SICI\)1099-1530\(199701\)8:1<91::AID-PPP238>3.0.CO;2-4](https://dx.doi.org/10.1002/(SICI)1099-1530(199701)8:1<91::AID-PPP238>3.0.CO;2-4), 1997.
- 950 Sanders, J. W., Cuffey, K. M., Moore, J. R., MacGregor, K. R., and Kavanaugh, J. L.: Periglacial weathering and headwall erosion in cirque glacier bergschrunds, *Geology*, 40, 779-782, <https://dx.doi.org/10.1130/g33330.1>, 2012.
- Sass, O.: Rock moisture measurements: techniques, results, and implications for weathering, *Earth Surface Processes and Landforms*, 30, 359-374, <https://dx.doi.org/10.1002/esp.1214>, 2005a.
- 955 Sass, O.: Spatial patterns of rockfall intensity in the northern Alps, *Zeitschrift für Geomorphologie, Supplementary Issues*, 138, 51-65, 2005b.
- Scherer, G. W.: Crystallization in pores, *Cement and Concrete Research*, 29, 1347-1358, [https://dx.doi.org/10.1016/S0008-8846\(99\)00002-2](https://dx.doi.org/10.1016/S0008-8846(99)00002-2), 1999.
- Scott, D. N. and Wohl, E. E.: Bedrock fracture influences on geomorphic process and form across process domains and scales, *Earth Surface Processes and Landforms*, 44, 27-45, <https://doi.org/10.1002/esp.4473>, 2019.
- 960 Sibley, D. N., Lombart, P., Noya, E. G., Archer, A. J., and MacDowell, L. G.: How ice grows from premelting films and water droplets, *Nature Communications*, 12, 239, <https://dx.doi.org/10.1038/s41467-020-20318-6>, 2021.
- Walder, J. and Hallet, B.: A Theoretical-Model of the Fracture of Rock During Freezing, *Geological Society of America Bulletin*, 96, 336-346, [https://dx.doi.org/10.1130/0016-7606\(1985\)96<336:ATMOTF>2.0.CO;2](https://dx.doi.org/10.1130/0016-7606(1985)96<336:ATMOTF>2.0.CO;2), 1985.
- 965 Walder, J. S. and Hallet, B.: The Physical Basis of Frost Weathering - toward a More Fundamental and Unified Perspective, *Arct. Alp. Res.*, 18, 27-32, <https://dx.doi.org/10.2307/1551211>, 1986.
- Wang, Y., Han, J. Q., and Li, C. H.: Acoustic emission and CT investigation on fracture evolution of granite containing two flaws subjected to freeze-thaw and cyclic uniaxial increasing-amplitude loading conditions, *Construction and Building Materials*, 260, 119769, <https://doi.org/10.1016/j.conbuildmat.2020.119769>, 2020a.
- 970 Wang, Y., Feng, W. K., Wang, H. J., Li, C. H., and Hou, Z. Q.: Rock bridge fracturing characteristics in granite induced by freeze-thaw and uniaxial deformation revealed by AE monitoring and post-test CT scanning, *Cold Regions Science and Technology*, 177, 103115, <https://doi.org/10.1016/j.coldregions.2020.103115>, 2020b.
- Webber, J. B. W., Dore, J. C., Strange, J. H., Anderson, R., and Tohidi, B.: Plastic ice in confined geometry: the evidence from neutron diffraction and NMR relaxation, *Journal of Physics: Condensed Matter*, 19, 415117, <https://dx.doi.org/10.1088/0953-8984/19/41/415117>, 2007.
- 975 Whalley, W. B., Rea, B. R., and Rainey, M. M.: Weathering, Blockfields, and Fracture Systems and the Implications for Long-Term Landscape Formation: Some Evidence from Lyngen and Øksfordjøkelen Areas in North Norway, *Polar Geography*, 28, 93-119, <https://dx.doi.org/10.1080/789610120>, 2004.
- Withers, P. J., Bouman, C., Carmignato, S., Cnudde, V., Grimaldi, D., Hagen, C. K., Maire, E., Manley, M., Du Plessis, A., and Stock, S. R.: X-ray computed tomography, *Nature Reviews Methods Primers*, 1, 18, 10.1038/s43586-021-00015-4, 2021.
- 980